CHAPTER 5

GROUND-PENETRATING RADAR (GPR) INVESTIGATIONS ALONG THE KACHCHH MAINLAND FAULT (KMF)

INTRODUCTION

The GPR has been proved as the most promising geophysical tool to image and detect the buried active faults and document the related subsurface deformational structures in diverse geological settings (Carpentier et al., 2012a, 2012b; Ercoli et al., 2014; Cinti et al., 2015; McBride et al., 2015; Pousse-Beltran et al., 2018; Lunina et al., 2016, 2020). A number of GPR-based studies combined with field data along major faults in the KRB have led to a significantly improved understanding of their nature and neotectonic history. From north to south, these include the KHF (Patidar et al., 2007, 2008), eastern part of the KMF (Chowksey et al., 2011a), VGKNFS (Shaikh et al., 2020), GF (Maurya et al., 2013), SWF (Maurya et al., 2017a), northern coast of the Gulf of Kachchh (Shukla et al., 2013) and an extensive review work carried out by Maurya et al. (2017b). The field and GPR based studies performed by Patidar et al. (2007), (2008), Chowksey et al. (2011a), (2011b) provided evidence of the thin Quaternary deposits cover concealing the KHF and the KMF and neotectonic evolution of the KMU as a result. Shaikh et al. (2020) used GPR in the KRB for the first time ever to image the numerous strands of deformation bands, which are the characteristics of deformed porous strata, exposed in the fault deformation zone of the VGKNFS. Trenching is an expensive way to collect data on seismogenic rupture parameters (Lunina et al., 2016, 2020). For structural and geomorphological studies, shallow geophysical approaches, particularly the GPR method, combined with natural outcrop interpretation to calibrate the geophysical details, can be considered as an alternative and a supporting tool for trenching (Lunina et al., 2016, 2020).

Faults can be readily detected on GPR sections if (i) different lithologies with/without varying amount of clay content are juxtaposed across the main fault plane, creating distinct radar facies between the hangingwall and footwall. The radar responses of varying lithologies can differ in terms of their amplitude, pattern, continuity and thickness. (ii) Continuous reflectors are disrupted and displaced significantly along steeply dipping discontinuities. (iii) Faults juxtapose strata with

varying dips, which generate significant changes in the reflectors geometry. This case has not been observed in the present study. Much of the reflectors are sub-horizontal but, if encountered by the fault plane, they obviously indicate offsetting, change in dip or disruption. Warping or dragging of reflectors is also noted.

In this context, the present study focuses on imaging and detecting the surface as well as shallow subsurface geometry of western part of the seismically active E-W to NW-SE striking KMF by means of field structural studies and GPR surveys. Because of the accessible patchy and isolated rock exposures, this area was selected for research. The prime concern was to evaluate from GPR cross-sections whether the impact of any Quaternary movements on the buried KMF could be detected by displacement and/or folding of the near-surface sediments. Shaikh et al. (2019) studied long-term landscape evolutionary history of western part of the KMF in response to uplift induced structurally controlled erosion due to periodic tectonic movement along the KMF. Cross-sections generated from GPR surveys by previous workers in the KRB revealed only the major blind active faults. Along with the detection of the major blind fault, associated deformational structures developed in the fault damage zone, off-fault folding, subsidiary antithetic and synthetic fault strands, subsurface fault zone stratigraphy are described. Conventional geological and paleoseismological studies have not detected these structures. In this contribution, with the aid of GPR images, a multitude of secondary active faults distributed in the KMF deformation zone are delineated. The study has implications for understanding neotectonic and seismic hazard estimation along the KMF.

GROUND PENETRATING RADAR (GPR) SURVEY METHODOLOGY

The GPR creates images of the subsurface that superficially mimic seismic reflection images (McCalpin, 2009). The comparisons derived from the common use of transmitted waves that are reflected, which are then detected on the surface by a receiver (McCalpin, 2009). Unlike compressional elastic waves used in seismic reflection survey, transmitted electromagnetic waves are used in GPR survey (McCalpin, 2009).

2D GPR is an effective shallow subsurface geophysical imaging technique to investigate the geological discontinuities such as faults, deformation bands, fractures and to characterize the deformed sedimentary structures associated with them (McClymont et al., 2010; Cinti et al., 2015; Lunina and Denisenko, 2020; Shaikh et al.,

2020). GPR uses the propagation, reflection and scattering of 10 MHz to 1000 MHz frequency electromagnetic (EM) waves in the Earth (Jol, 2009). The method depends upon the dielectric properties of the rock interfaces in the subsurface (McCalpin, 2009). The depth of the investigation depends on the degree of attenuation of EM waves with depth and the antennae frequency used. The lower the frequency, the greater the penetration depth, which varies from a few centimeters in conductive materials up to 50 m for low conductivity media (Davis and Annan, 1989; Jol, 2009).

According to published literature and detailed field investigations carried out in the present study, the KMF, which is acting as the lithotectonic contact between the rocks of Mesozoic sandstone/shale and Tertiary limestone, is buried below the Quaternary deposits cover (Maurya et al., 2003). While the W-, NW-, NNW- and NE-striking intra-domal and inter-domal faults with oblique slip-sense are well-exposed in the study area. Therefore, high-resolution 2D GPR data were recorded along pre-defined transects perpendicular to the KMF strike (i) to detect the position and geometry of the KMF buried below Quaternary sediments cover, (ii) to map the continuity of the KMF and, (iii) to understand sub-seismic characteristics of the KMF and distribution of secondary faulting within the deformation zone. The GPR surveys were planned in a systematic manner, which covers multiple locations of data acquisition based on field mapping of neotectonic and geomorphic evidence. The planned survey sites are located between Lakhpat in the west and Manjal dome in the east. Finally, the good quality GPR profiles from various survey sites were selected, which are presented and interpreted in terms of the near-surface fault properties of the KMF.

GROUND PENETRATING RADAR (GPR) STUDIES ALONG KACHCHH MAINLAND FAULT (KMF)

The W, NW, NNW and NE striking intra-domal faults with normal slip are well-exposed. While the KMF, which is identified as the lithotectonic contact between the rocks of Mesozoic sandstone and Tertiary limestone and shale (Biswas, 1993; Chowksey et al., 2011a, 2011b; Maurya et al., 2017), is located north of the scarps and is buried below the Quaternary deposits cover. Therefore, to map the continuity of the KMF and to understand its shallow subsurface characteristics, GPR surveys were carried out. Radargrams are presented and interpreted in terms of the near-surface fault properties of the KMF.

Acquisition of geophysical data

The radargrams were obtained by using three different frequency antennas – unshielded bistatic 35 MHz and 80 MHz and shielded monostatic 200 MHz with single-channel Subsurface Interface Radar-20 (SIR-20) system manufactured by GSSI Inc. USA. The 200 MHz frequency antennas provided satisfactory results in terms of depth of penetration and data resolution required to study the near-surface nature of the fault. Radargrams collected from 200 MHz antenna were acquired in continuous mode by connecting to the survey wheel. Whereas, radargrams taken from 80 and 35 MHz bistatic antennas were collected in point mode. Several profiles were collected along the same transect to determine the most suitable header parameters for the particular terrain. During the survey, the marker was assigned manually to the radargram at an inferred location of the fault. This allowed us to determine the approximate position of the fault in the radargram. The fault position was further confirmed by observing the changes in the reflector patterns and the field check was done to observe the surface impression. The dielectric constant was kept at 7 with time window varied from 100–500 ns depending on the antenna used. Several Common Mid-Point (CMP) gathers were acquired at each site to estimate the velocity of propagation of EM waves. The GPR surveys were conducted well away from trees and power lines running parallel to the road at the end of the agricultural field that could affect the quality and interpretability of the profiles.

Processing of GPR data

Few radargrams recorded were severely affected by high-frequency snow-like noise, which is prevalent at greater depths, masking the real reflections to a great extent. In some cases, sharp vertical bands of low-frequency had influenced the radargrams. The GPR data collected often show long, continuous flat reflectors of system ringing noise may be due to instability of the equipment during dragging and vibrations during survey operations (Green et al., 2003; Shan et al., 2015). Therefore, processing of raw radargrams was required as the data were affected by different kinds of noises.

The post-survey processing of GPR data was performed in RADAN (v.7) software by GSSI Inc. The noise was removed by following standard processing steps and to obtain the best visual representation of radargrams to appreciate and interpret the geological features under investigation. The basic processing steps followed are – time-

zero correction, background removal, band-pass frequency filtering and range gain (Jol and Bristow, 2003; Cassidy, 2009; Jol, 2009).

(i) Time-zero correction: The vertical position of the radargram was adjusted to remove the delay time and to match the surface position (Cassidy, 2009). The purpose of doing time-zero correction is to get the accurate depth of the reflectors because now the topmost scan of the radargram is in close approximation with the ground surface. Whereas, few radargrams were kept unchanged to compare the dipping reflectors with the horizontal direct reflections at the top.

(ii) Background removal: Few radargrams were affected by continuous, flat-lying reflectors of ringing noise. Also, the initial data are dominated by direct air and ground waves at early times (Green et al., 2003). The full pass background removal filter was applied to suppress the strong low-frequency background noise (Carpentier et al., 2012b; McBride et al., 2015; Pouse-Beltran et al., 2018).

(iii) Band-pass filtering: The vertical and horizontal band-pass filters were applied using Finite Impulse Response (FIR) and Infinite Impulse Response (IIR) Filters to exclude low- and high-frequency noise, which improved signal/noise ratio significantly (Lacan et al., 2012). The vertical low-pass and high-pass FIR filter of 300 and 50 MHz cut-off frequency, respectively, reduced high-frequency noise and low-frequency modulation above and below the established threshold to a great extent. A 3–7 scans IIR horizontal low-pass smoothing filter was applied to further smooth the radargram and to remove the sharp low-frequency vertical bands.

(iv) Topographic correction: As most of the profiles were taken on flat terrain, there was no need to correct for the elevation differences except the profile acquired to the north of Mundhan anticline.

(v) Range gain: The function was applied to compensate for the attenuation caused during processing methods like background removal and to improve the visibility of reflectors mostly located in the lower section of the profiles (Christie et al., 2009). The unnecessary information during the dead time at the beginning and end of the radargram (occurs when the antenna is stationary and running in continuous mode) was removed by selecting and cutting undesired blocks.

(vi) Semblance analysis: The CMP gathers were used to determine the subsurface velocity for time-depth conversion. A relatively constant velocity of 0.12 m ns^{-1} was obtained due to sand dominated subsurface lithologies.

Velocity analysis

The subsurface EM waves velocity is important for conversion of two-way travel time (TWTT) to accurate estimation of depth (Neal, 2004). The standard approach to estimate the EM wave velocity is to carry out the CMP survey (Neal, 2004). The CMP survey works on the principle of Normal Move Out (NMO) as in seismic reflection survey (Neal, 2004). Several CMP gathers were acquired using 80 MHz antenna to estimate the propagation velocity of Electro-Magnetic (EM) waves in the subsurface (Fig. 5.1).

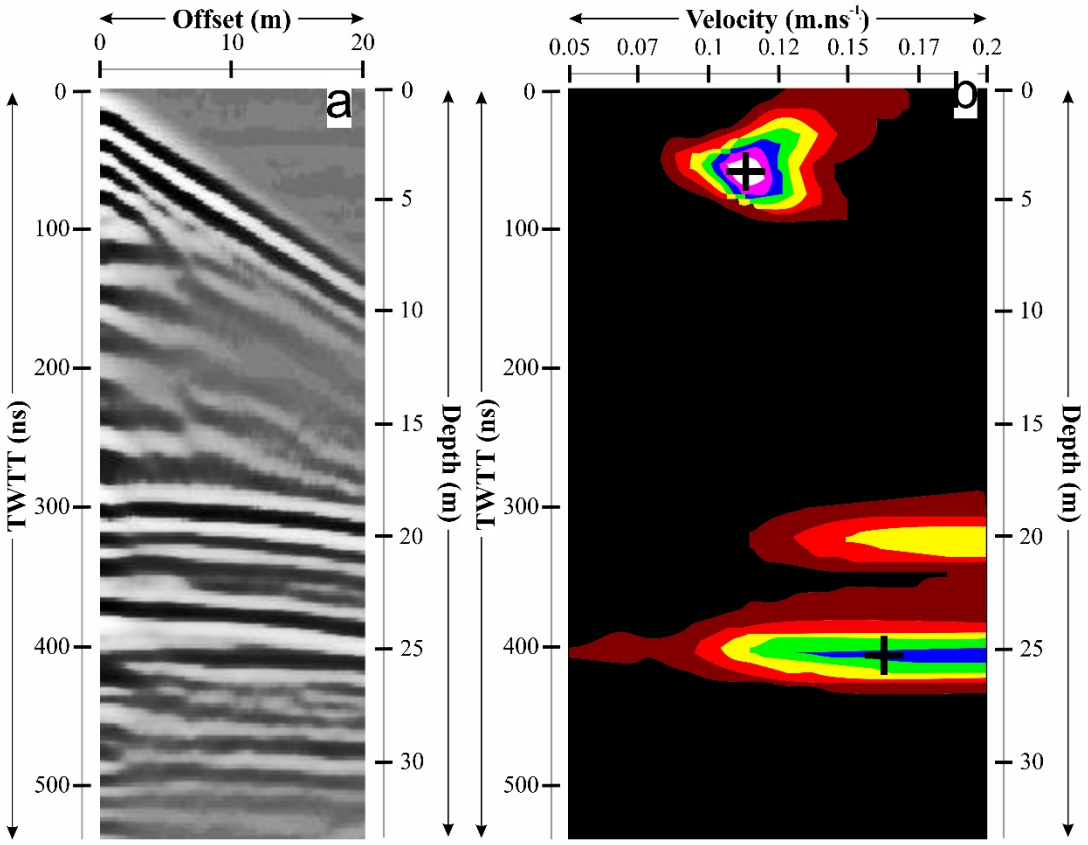

Fig. 5.1. Processed common mid-point (CMP) profile and related semblance plot.

The CMP surveys have been carried out well away from the deformation zone of the fault so that the reflection events can be obtained from the beds which are undeformed in the subsurface and are horizontal in the plane of survey. The CMP data is recorded at multiple offsets using bi-static antennae configuration. At first, the transmitting and receiving antennas are begin to operate at zero-offset/initial offset position. The initial offset is kept 1 m between the centerline positions of transmitting and receiving antennas. Data are then collected at multiple offsets by moving apart both

the antennas from the zero-offset position with the step size of 10 cm. CMP data are collected up to the total offset of 20 m horizontal distance.

The dielectric constant/relative permittivity (εr) of Bhuj/Jhuran sandstone can be calculated once the average velocity of EM waves is known. Once the average velocity is calculated, the CMP profile analysis is then performed for accurate time-depth conversion and migration algorithms. The velocity analysis computes the velocity spectrum/semblance plot. It shows signal coherency in the form of a graph of velocity versus two-way zero-offset time.

The individual reflection events are picked manually and the estimated velocity was derived from the semblance plot (Fig. 5.1). The average velocity of 0.12 m ns^{-1}, corresponding to a dielectric constant of 7, is estimated through CMP profile analysis. This value has been used for time to depth conversion of all the GPR profiles collected. The average constant velocity has been used to perform migration on some of the 2D profiles and it reduced the noise significantly and generated the most accurate images.

GPR amplitude analysis

The sedimentary facies associations of the Mesozoic Jhuran and Bhuj Formation and, Tertiary rocks have been widely discussed by previous workers (Biswas, 1993, 2016). Chowksey et al. (2011a), (2011b) discussed in detail the Quaternary stratigraphy exposed in the eastern KMF. They are found to be useful to understand the exposed stratigraphic sequences in the western KMF and to correlate them with the GPR radar facies. A radar facies is characterized as a three-dimensional body/zone with similar radar reflection patterns that is bordered by radar surfaces and imaged along two-dimensional profiles (Shan et al., 2015; Berton et al., 2019). The radar facies are described in terms of continuity and shape of reflectors, amplitude response characteristics, internal reflection configuration and external package geometry (Jol and Bristow, 2003; Magalhães et al., 2017). It is also important to identify reflectors termination pattern such as truncation, onlap and downlap (Berton et al., 2019).

The depth-wise decay in GPR positive amplitude response is discussed. Positive amplitudes were picked from selected portions of each of the GPR sections. By picking the maximum radar amplitude of Quaternary deposits, Mesozoic and Tertiary rocks, the radar response characteristics of different stratigraphic units were understood. The values of relative amplitude were noted down at regular depth intervals.

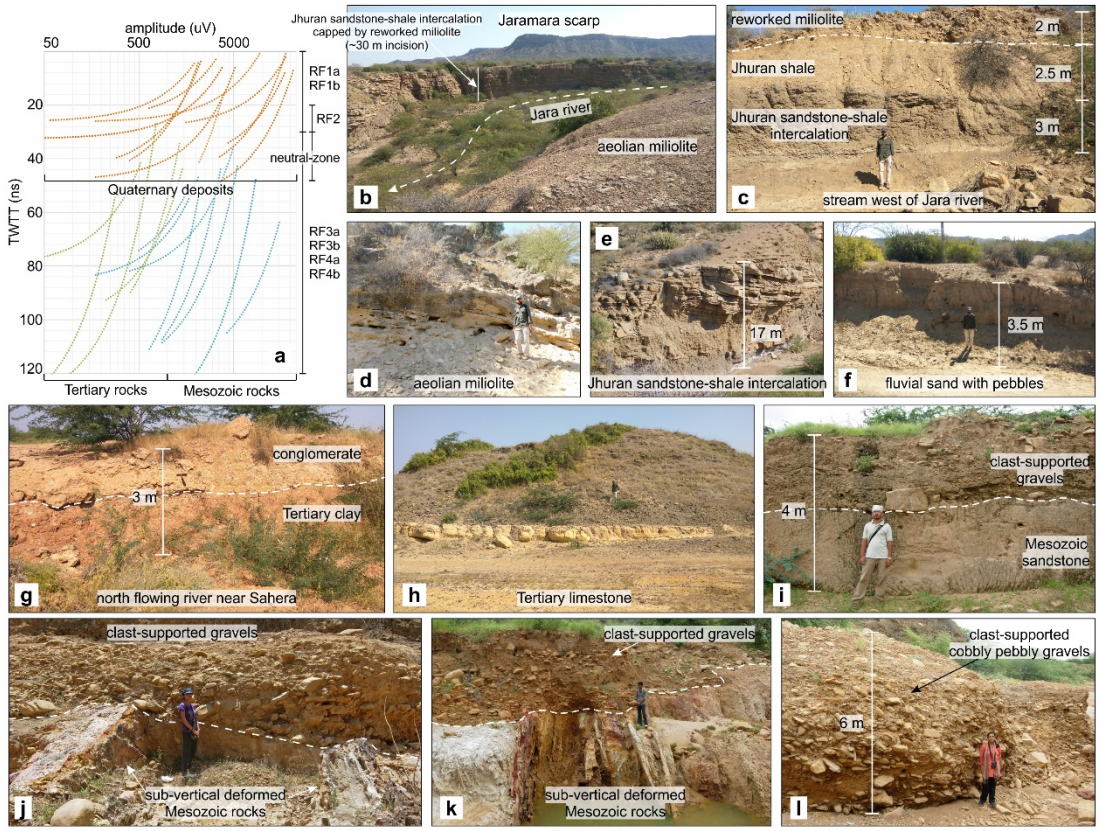

Fig. 5.2. (a) Plot showing depth-wise decay in radar amplitude responses. Logarithmic upper axis shows radar amplitude in uV and left axis shows two way travel time (TWTT) in ns. Orange curves for Quaternary deposits, green for Tertiary rocks and blue for Mesozoic rocks. (b) At the southern margin of the Jara dome, view of the Jara river facing south. (c) ~7.5 m high incised cliff of a stream west of Jara river. Thin-bedded Jhuran sandstone-shale intercalation is capped by 2 m thick colluvio-fluvial miliolite deposits. (d) Quaternary aeolian miliolite deposits showing large-scale cross-stratification. (e) Incised cliff of ~17 m high Jara river exposing thinly bedded Mesozoic Jhuran sandstone-shale intercalated rocks. Note the trough cross-stratification in the upper parts of the river cliff section. (f) ~3.5 m high cliff of a small tributary of the stream west of Jara river. (g) ~3 m high cliff section of north flowing river near Sahera exposing conglomerate deposits underlain by Tertiary clay deposits. (h) A mound of Tertiary limestone in the vicinity of the Karanpur dome. (i) ~4 m river cliff section exposing thick clast-supported gravels resting unconformably over undeformed Mesozoic sandstones. (j) and (k) Clast-supported gravels resting unconformably over near vertical, deformed Mesozoic sandstones in Falay river. (l) ~6 m thick coarse, angular clast-supported gravels in Falay river.

With such obtained values, it is possible to divide the GPR sections into radar facies – Quaternary deposits into radar facies RF1a, RF1b (up to 20–30 ns depth) and RF2 (between 20–30 ns depth) (Maurya et al., 2009; Khonde et al., 2011), Mesozoic rocks into RF3a and RF3b (from 25–30 ns downward), Tertiary rocks into RF4a and

RF4b (from 25–30 ns downward). The results of the radar amplitude analysis performed are demonstrated in Fig. 5.2. The logarithmic function is fitted with the data, which shows depth-wise decay in amplitude response. Multiple logarithmic curves can be distinguished into orange curves for the unconsolidated colluvio-fluvial deposits of Quaternary age (50–7000 uV amplitude range), green curves for Tertiary rocks (50–600 uV amplitude range) and blue curves for Mesozoic rocks (600–7000 uV amplitude range). As can be seen in the Fig. 5.2, the sediment-bedrock interface is generally encountered at 30–50 ns depth. Tertiary rocks are marked by low-amplitude responses while the sand/shale dominated stratified Mesozoic siliciclastic rocks are characterized by comparatively high-amplitude responses. The Quaternary colluvial deposits are marked low- to moderate-amplitude responses and the deposits range from poorly sorted, matrix-supported deposits to moderately sorted, pebbly clast-supported deposits (Chowksey et al., 2011). This general outline was used for GPR data interpretation in the present study and to distinguish the subsurface stratigraphy, which was supported by field observations.

Fig. 5.2 shows the variety of lithological units exposed in the NHRFZ. Note that the GPR data acquisition sites are farther north from the location of cliff exposures shown in Fig. 5.2. Such lithology is still exposed at the location of GPR data acquisition, but it is now buried by Holocene Rann sediments cover. The Jara river originates from the backslope of the Jaramara scarp and meets the Banni plain in the north (Shaikh et al., 2019). The river is incised by ~30 m into the Mesozoic Jhuran sandstone-shale intercalation overlain by fluvially reworked miliolites, deposited over an erosional surface (Fig. 5.2b). The post-miliolite river incision over the Jara dome can be observed in the low undulating topography. Notice the exposure of an aeolian miliolite in the foreground and appearance of the Jaramara scarp in the background (Fig. 5.2b). The stream west of Jara river flows in the low hilly topography of the Jara dome (Shaikh et al., 2019). The incised cliff of the river exposes ~2 m thick clast-supported colluvio-fluvial Quaternary miliolite deposits covering the top surface (Fig. 5.2c). It is underlain by ~5.5 m thick thinly-bedded Jhuran sandstone-shale intercalated deposits. In the vicinity of the Jaramara scarp, the north-flowing Jara river has formed a deep gorge (Shaikh et al., 2019). In the gorge reach, ~10 m thick Quaternary aeolian miliolite deposits capping the Mesozoic Jhuran sandstone and shale are exposed (Fig. 5.2d) (Shaikh et al., 2019). ~1.5 km west of the inter-domal saddle occupied by Ukra intrusive, the Jara river shows ~17 m deep incision in Mesozoic Jhuran sandstone-shale

intercalated rocks (Fig. 5.2e). Note that the cliff section is devoid of Quaternary miliolite capping. A small tributary of the stream west of Jara river exposes fluvial sand with pebbles overlying the Jhuran shale in lower parts of the cliff section (Fig. 5.2f). Near Sahera, ~3 m high cliff of a river flowing west of Mundhan anticline shows conglomerate exposure underlain by Tertiary clay deposits (Fig. 5.2g). Tertiary limestone rocks are exposed in the form of a mound near the Karanpur dome (Fig. 5.2h).

The cliff sections of rivers that pass through the eastern NHRFZ are also observed, which lie outside the study area. It is important to understand the lithological heterogeneity in the KMF zone and to identify various radar facies. In contrast to the western NHRFZ, a thick succession of Quaternary colluvial deposits are found in the north-flowing rivers in the eastern NHRFZ, in front of the ~W-striking KMF scarp. In the KMF deformation zone, the vertically dipping Mesozoic sandstones are unconformably covered by the colluvio-fluvial deposits consisting of coarse-grained clast-supported gravels in the Falay river (Figs. 5.2i, j) (Chowksey et al., 2011b). Because the electrical impedance contrast is strong between the Quaternary deposits and underlying Mesozoic/Tertiary rocks, the GPR signals notably reflect off from such unconformable boundaries. Tens of metres wide highly sheared near-vertical Mesozoic sandstone underlie the Quaternary clast-supported gravel deposits (Fig. 5.2k) (Chowksey et al., 2011b). Unsorted colluvial deposits mainly consisting of highly angular clast-supported cobbly pebbly gravel deposits were observed in Falay river (Fig. 5.2l) (Chowksey et al., 2011b). The scarp-derived extremely angular, poorly sorted and varied scale of clasts indicate a very short transportation history in front of the KMF scarp. Chowksey et al. (2011b) inferred that the colluvium was formed from the pre-existing KMF scarp comprising Mesozoic sedimentary rocks, in response to the neotectonic uplift along the KMF. The produced colluvial material was then reworked by fluvial agencies and redeposited it over the present-day KMF, north of the paleo-KMF scarp. It is assumed that in the western part of the KMF, similar conditions still existed, but later on, they were covered by Holocene Rann sediments.

GPR ATTRIBUTE ANALYSIS

Some radargrams were further processed with Hilbert transform using the magnitude attribute (instantaneous amplitude) and instantaneous phase attribute. The magnitude display is useful for illustrating the raw energy reflected from the subsurface strata. Envelope (instantaneous amplitude) calculates the absolute value of each wavelet

by converting negative wavelets to positive wavelets, resulting in a positive mono-pulse wavelet. This process was used by observing the signal strength and reflectivity to detect the energy loss that happens when highly deformed fault zone is encountered in radargram. The results were more sensitive to detect the fault plane based on magnitude data rather than amplitude information (Cassidy, 2012). The use of trace envelope superimposition over wiggle trace and phase attribute has greatly enhanced the structural interpretation of radargram (Cinti et al., 2015). The instantaneous phase attribute gives equal strength to weak and strong reflections and thus emphasizes the discontinuity of reflectors in terms of faults (Zhao et al., 2015). To illustrate the discontinuities with the energy distinct on either side of them, the Hilbert transform using magnitude attribute was applied (Lunina et al., 2016).

The instantaneous phase attribute can be used to denote the lateral continuity of the lithology. Sudden changes in the phase attribute, therefore, highlights the presence of subsurface discontinuity. The phase information is useful in delineating structural features such as faults, onlaps and prograding reflections.

GPR IMAGING INTERPRETATION

Depending on the frequency and orientation of the survey antenna, the heterogeneity of the fault material and width of the fault damage zone; major and other subsidiary faults generate a variety of signatures on GPR radargrams (Green et al., 2003 and references therein). Keeping these points into account and thoroughly analyzing each of the radargrams, it is inferred that the KMF and associated subsidiary slip planes cannot be mapped in the shallow subsurface solely on the basis of GPR data. As a result, by verifying the GPR data with the outcrop exposures of KMF wherever available, the GPR sections are interpreted.

The results of GPR profiles from different survey sites along the KMF are presented and discussed. For more detailed representation of radargrams, the plot format varies between wiggle traces overlapped by lithology, wiggle traces overlapped by magnitude attribute, uninterpreted linescan plot and interpreted linescan plot. The raw profiles were 70-80 meters long, but only an interesting portion of the full profiles is displayed. In all the cases, the fault zone has been identified by observing the radar signatures such as, the abrupt lateral change in amplitude, sudden truncation of reflectors, regions with high energy loss (high signal attenuation) that are well recognized criteria for detecting faults with lithological contrast (Anderson et al., 2003;

McClymont et al., 2008a, 2008b; Cinti et al., 2015; Shaikh et al., 2020). On the basis of variation in radar reflection patterns, radargrams are divided into several zones of distinct radar facies, which are discussed in the following sub-sections. Much of the radar facies interpretation is based on the surficial field observations and Quaternary stratigraphic units exposed in the study area or along the eastern part of the KMF. Because of the significant difference in the composition of Mesozoic and Tertiary rocks, the radar signatures of the both the rock types exhibit large variance in each of the GPR profile recorded across the KMF. The GPR plots presented have no vertical exaggeration and, therefore, the true dip of reflectors is shown.

Because the KMF damage zone is highly brittle deformed, it is profoundly impacted by multiple antithetic and synthetic discontinuities in large amounts. In each of the radargrams recorded in the deformation zone of KMF, numerous sub-vertical faults/discontinuities with/without displacement are identified, which are all confined to the upper crustal parts. In the western part of the KRB, It is very important to develop their relationship with the general structural pattern of the KMF. The upper few meters of all the radargrams are occupied by Quaternary deposits. The Quaternary deposits are base-of-scarp colluvial deposits, which have been eroded from the KMF scarp and deposited in the footwall. Thus, the shallow subsurface geophysical surveys allowed us to verify the presence of the Quaternary deposits in the downthrown block of the KMF.

Site 1

The GPR data at site 1 was collected SE of Karanpur dome to the westernmost part of the study area (Fig. 5.3). Almost vertical nummulitic limestone beds of Eocene age striking N105° and highly sheared Mesozoic sandstone with near-vertical dip are exposed. The contact between the Mesozoic and Tertiary rocks marks the surface position of the NNW striking KMF. The GPR survey was carried out over a 22 m long transect in N40° orientation using a 200 MHz antenna across the litho-tectonic contact marking the trace of the KMF.

The interpreted processed radargram depicts the following radar facies – *(i) RF3a (Mesozoic sandstone)*. On the SW side, at ~20–95 ns depth, high amplitude cycles with thick, dense horizontal reflections of RF3a are observed. They correspond to the highly compacted Mesozoic sandstone located in the upthrown block of the KMF (marked by dark green lines in Fig. 5.3b). Phase-based attribute in Fig. 5.3c show high-energy contours corresponding to the Mesozoic sandstones. Broken, low amplitude

reflections of RF3b are lacking in the radargram. *(ii) RF4a and RF4b (Tertiary limestone).* The weak amplitude returns with successively increasing dip radar facies characterize RF4a of Tertiary limestone on the NE side of the radargram (Fig. 5.3a, b). RF4b is characterized by low-amplitude, discontinuous, chaotic reflections representing clay-rich, massive limestone deposits, located towards the downthrown block of the KMF (Fig. 5.3a, b).

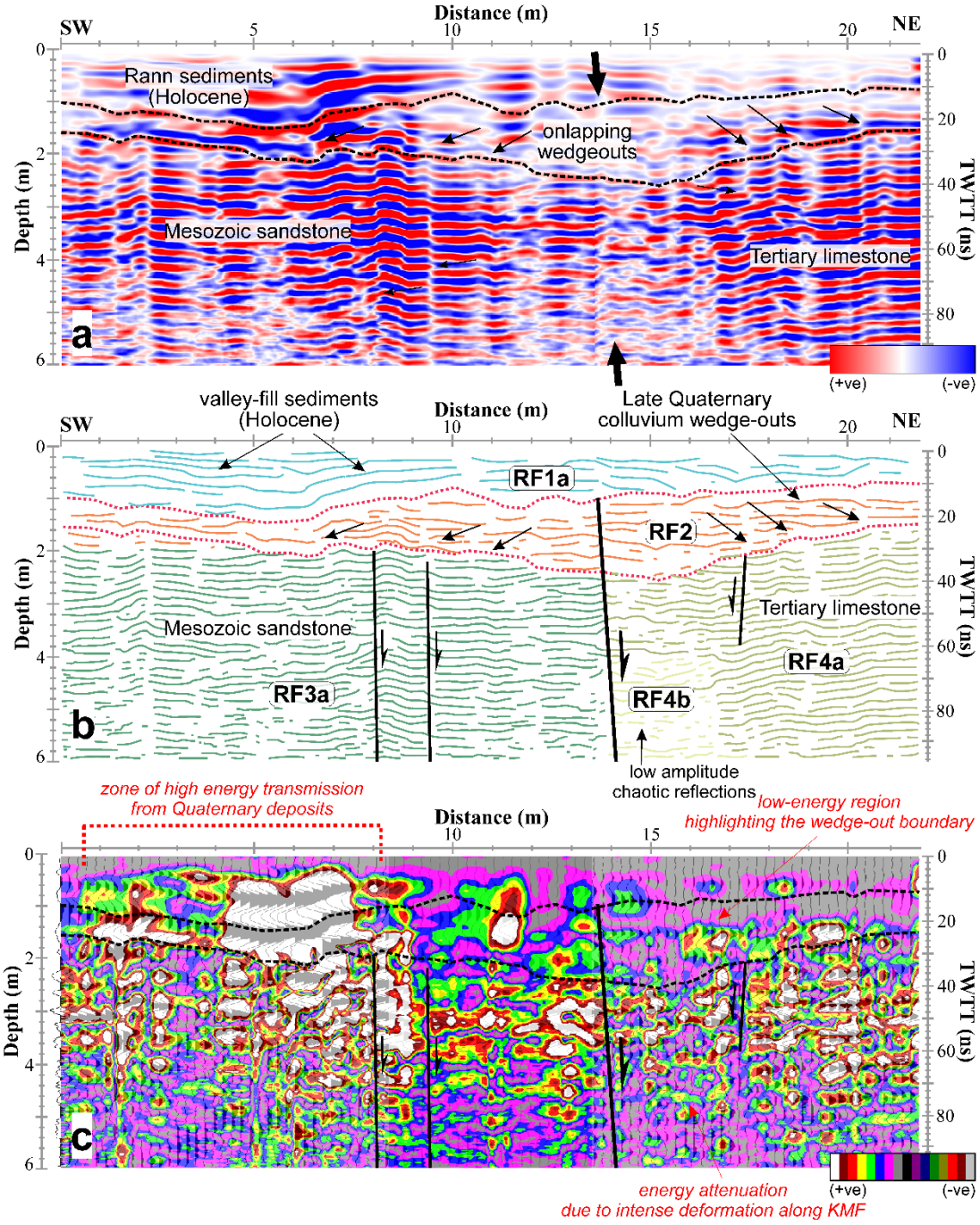

Fig. 5.3. 22 m long, NE oriented GPR section acquired across the KMF, between Karanpur dome and western flank of Ghuneri dome at site 1. Transect is taken over flat soil surface. See geological map of the study area in Fig. 3.1 for the location of GPR survey site. Axis on left side shows penetration depth in meters and on right side two way travel time (TWTT) in ns is denoted. The upper axis shows section length in meters. Based on average subsurface radar wave velocity of 0.12 m ns^{-1}, radar arrivals have been translated to time-depth. Note that the direct air and ground waves have been muted in each of the plot formats. (a) Interpreted linescan plot. GPR amplitudes are represented by red (positive) and blue (negative) reflectors. Large arrows indicate the projected location of the KMF. Smaller arrows mark the interpreted position of secondary slip planes. Black dashed lines indicate conformable and non-conformable contacts between individual lithounits. (b) Interpreted sketch with lithology represented by colored lines. From top to bottom, based on the reflectors response pattern, the cross-section is divided into radar facies RF1a – uppermost Late Quaternary valley-fill deposits, RF2 - Early Quaternary colluvium wedge-outs, RF3a - Mesozoic sandstone, RF4a and RF4b - Tertiary limestone deposits. Note the presence of Early Quaternary wedge-shaped deposits with onalpping and pinch over reflectors that terminate against the disconformable sediment (RF2)-bedrock (RF3a and RF4a) interface. (c) Trace envelope based on magnitude draped over wiggle traces. The color scale reflects the energy continuum, with white contours representing the highest-energy regions, while the lowest-energy regions are represented by grey contours. The lateral energy changes of EM waves clearly marks the presence of fault planes. Black lines indicate fault planes and half-arrows denote movement direction of the upthrown block in Figs. (b) and (c). The KMF with revere slip can be easily appreciated due to strong attenuation contrast and clear lateral discontinuity of the reflectors between 13–15 m distance. Note the offset of continuous reflectors occurs in RF3a and RF4a, and correspond to secondary, synthetic and antithetic slip planes with normal slip.

Magnitude-based attribute in Fig. 5.3c denote scattered, low-energy contours of RF4a and RF4b as compared to high-energy contours of RF3a. *(iii) RF1a (Younger valley-fill deposits).* RF1a characterizes the Late Quaternary valley-fill sediments capping the underlying rocks (Fig. 5.3b). *(iv) RF2 (Colluvial wedge-outs).* The wedge-out geometry, which encompasses semi-continuous to chaotic reflections pattern, can be clearly observed in the interpreted sketch and in the magnitude attribute plot as it encloses the low-amplitude zone (Fig. 5.3a, b, c). The wedge-out comprises Late Quaternary valley-fill deposits e.g., miliolitic sands, scree deposits, conglometic boulders, coarse sandy material etc. The jumbled up material will essentially give chaotic reflection pattern which lacks sedimentary layered stratification. The reduction in thickness of sediments on both sides from the central part, covering the whole width of the radargram, indicate that the colluvial wedge dies away from the main fault. The

warping of reflections of RF1a and RF2 representing the Quaternary sediments can be observed from 5–10 m horizontal distance. The warped reflectors are marked by high-energy contours shown in magnitude-based attribute in Fig. 5.3c.

The southern side shows high amplitude cycles with thick, dense horizontal reflection events corresponding to the highly compacted baked Mesozoic sandstones as compared to the low, weak amplitude returns with successively increasing dip radar facies of Tertiary limestones on the northern side of the radargram (Fig. 5.4a, b, c). The Hilbert transform based on magnitude lapped over wiggle trace reveals ~5-7 m wide low-frequency subsurface anomaly in the radargram indicating the presence of the fault zone (Fig. 5.4a).

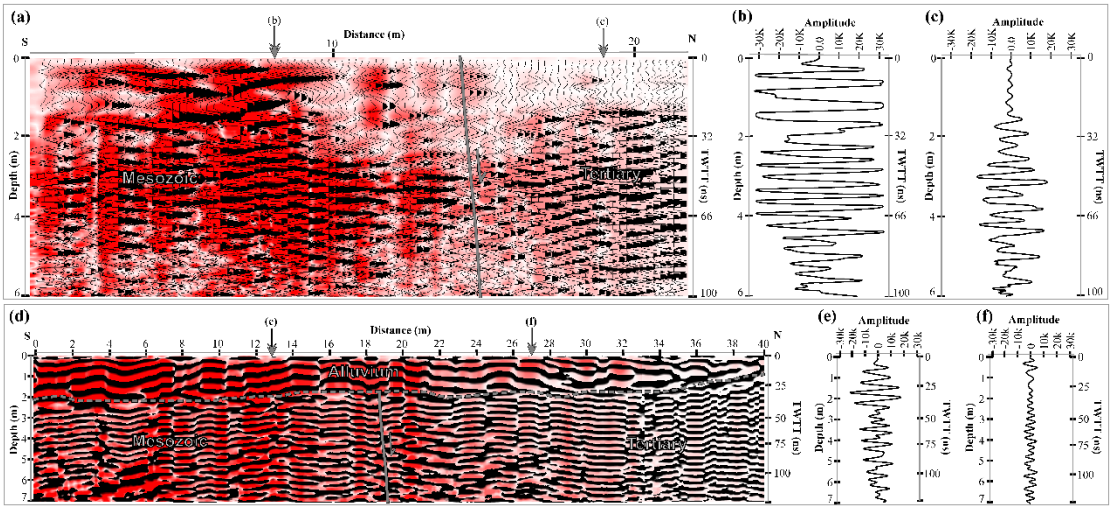

Fig. 5.4. Processed GPR radargrams (a) trace envelope based on magnitude draped over wiggle traces from 200 MHz antenna recorded across the KMF line at SE of Karanpur dome (site 1), location of site is shown in Fig. 3.1. The fault can be easily appreciated due to strong attenuation contrast and clear lateral discontinuity of the reflectors between 12 m to 16 m distance. The inferred highly steep normal fault is placed at 14 m distance. Down arrows at the top of profile (marked as (b) and (c)) indicate the position of single scan in oscilloscope format. (b) and (c) shows the individual reflected waveform from Mesozoic rocks and Tertiary rocks respectively. (d) trace envelope based on magnitude draped over trace envelope based on phase acquired from 200 MHz antenna recorded across the KMF line between Ghuneri dome & Karanpur dome (site 2), location of site is shown in Fig. 3.1. The high amplitude reflectors at the top of profile represent 1.5 to 2 m thick Quaternary alluvial cover. The KMF is inferred to be a high angle normal fault at ~ 20 m distance considering truncation of reflectors, change in dip and distortion of reflectors along the fault plane. Also note the strong attenuation contrast towards north for Tertiary rocks reflected by a pale red color of trace envelope based on magnitude. (e) and (f) shows the respective single scans for Mesozoic and Tertiary rocks.

The poor reflection events, high signal attenuation and relatively “transparent” zone identified from the Hilbert transform may be caused due to extreme energy loss in the fault zone due to intense deformation of the lithology. Both the radar facies are truncated at the fault zone indicating termination of strata. The KMF trace is marked by an abrupt amplitude decrease in between the two sets of radar facies at a distance of 14 m. It is inferred from the processed radargram that the KMF is a steep north dipping normal fault at SE of Karanpur dome. The interpretations are verified by nearby exposure of the fault partially covered by tilted miliolite deposits on a small hump.

Tectonic interpretation. ~5–7 m wide low-frequency subsurface anomaly, mostly occupied by RF4b, indicates the presence of the fault zone. The subsurface presence of the KMF is marked by – (i) truncation and abrupt amplitude decrease of reflectors of RF3a and RF4b along the KMF (Fig. 5.3a, b). Identity of KMF is lost in the phase-based attribute. (ii) Magnitude-based attribute highlights poor reflection events, high signal attenuation (Lacan et al., 2012) (Fig. 5.3c). The relatively “transparent” zone indicate extreme energy loss in the KMF zone due to intense deformation of the lithology (Fig. 5.3c). (iii) The colluvial wedge, which is the compelling proof to assess the presence of fault plane. It can be inferred that the colluvial wedges were collapsed from the paleo KMF scarp (Fig. 5.3b). It is inferred from the processed radargram that the KMF is a steep NE dipping normal fault at SE of Karanpur dome. The interpretations are verified by nearby surficial exposure of the fault partially covered by tilted miliolite deposits on a small hump. It is to be noted that the KMF does not propagate upwards into the Late Quaternary deposits of RF1a. The phase-based attribute revealed several synthetic and antithetic slip planes with normal slip in the deformation zone of the KMF. These slip planes are exposed in RF3a and RF4a and do not propagate upwards into Quaternary deposits represented by RF1a and RF2.

Site 2

Site 2 is located between Kranpur dome and western flank of Ghuneri dome (Fig. 3.1). Almost vertical nummulitic limestone beds of Eocene age are exposed striking N105°. Highly sheared vertically dipping Mesozoic sandstones are also exposed. Both the rock types are covered by patches of 1–2 m thick Quaternary alluvial cover. The lithotectonic contact between the Mesozoic and Tertiary rocks is marked by the presence of fault gouge as cohesionless, unconsolidated, red powdery material,

which marks the surface position of the KMF. The GPR survey was conducted using 200 MHz antenna on a flat ground.

The radargram shows the trace envelope using magnitude function lapped over a trace envelope based on cosine phase (Fig. 5.4d). The southern side of the radargram shows dense, strong amplitude reflections from the Mesozoic sandstones while the northern side of the radargram shows low, weak amplitude reflections from Tertiary limestones (Fig. 5.4d, e, f). The sudden truncation of reflectors, abrupt change in dip of the continuous reflectors, thinning-thickening of the reflectors mark the position of the KMF line at ~20 m horizontal distance. The KMF as seen in this radargram is inferred as a north-dipping normal fault to the NW of Ghuneri dome.

The southern side of the radargram shows dense, strong amplitude reflections from the Mesozoic sandstones, while the northern side shows low, weak amplitude reflections from Tertiary limestones (Fig. 5.5). The interpreted processed radargram depicts the following radar facies.

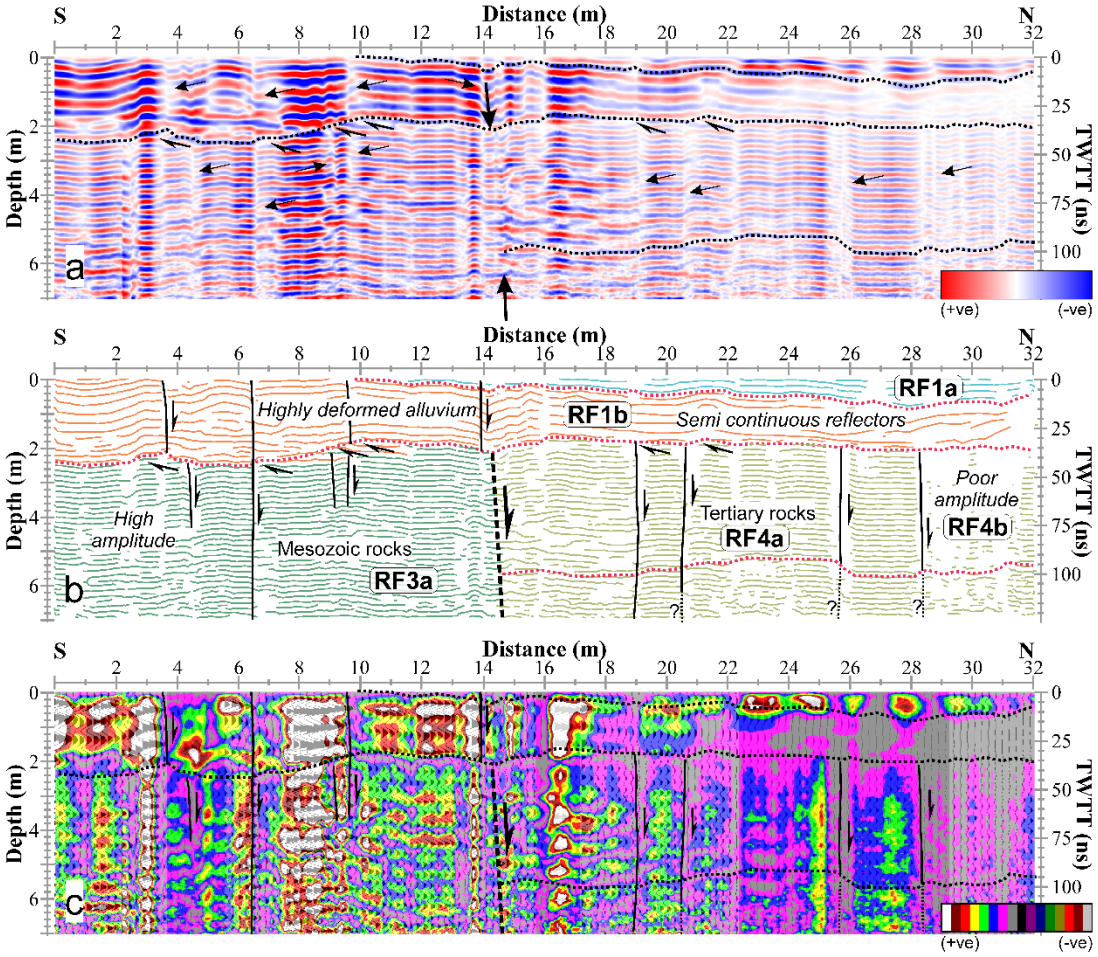

Fig. 5.5. 32 m long, north oriented GPR data recorded between Karanpur dome and western flank of Ghuneri dome at site 2. Axis on left side shows penetration depth in meters and on right side two way travel time (TWTT) in ns is denoted. The upper axis shows section length in meters. Based on average subsurface radar wave velocity of 0.12 m ns^{-1}, radar arrivals have been translated to time-depth. Note that the direct air and ground waves have been muted in each of the plot formats. (a) Interpreted linescan plot. GPR amplitudes are represented by red (positive) and blue (negative) reflectors. Large arrows indicate the projected location of the KMF. Smaller arrows mark the interpreted position of secondary slip planes. Black dashed lines indicate conformable and non-conformable contacts between individual lithounits. (b) Line drawing of Fig. (a) with colors highlighting different radar facies. Radar facies RF1b – Late Quaternary deposits with moderate to low-amplitude long continuous reflections. Black lines mark the interpreted position of secondary slip planes. Dashed lines indicate conformable and non-conformable contacts between individual lithounits. (c) Trace envelope based on magnitude draped over wiggle traces. The color scale reflects the energy continuum, with white contours representing the highest-energy regions, while the lowest-energy regions are represented by grey contours. The lateral energy changes of EM waves clearly marks the presence of fault planes. Black lines indicate fault planes and half-arrows denote movement direction of the upthrown block in Figs. (b) and (c). See geological map of the study area in Fig. 3.1 for the location of GPR survey sites. The steep northward dipping KMF with normal slip is inferred based on truncation and displacement of continuous reflections at ~15 m horizontal distance. Magnitude-based attribute in Fig. c clearly demonstrate two different lithologies, Mesozoic sandstone (high-energy contours of RF3a) in hangingwall and Tertiary limestone (low-energy contours of RF4a and RF4b) in footwall, are in lithotectonic contact due to tectonic movement along the KMF. Almost vertical slip planes with normal slip are interpreted from the radargram.

(i) RF3a (Mesozoic sandstone). High amplitude horizontal reflections of RF3a are observed on the southern side at ~30–125 ns depth (Fig. 5.5a, b). They lead to the strongly compacted Mesozoic sandstone. In the radargram, broken, low amplitude reflections of RF3b are absent. *(ii) RF4a and RF4b (Tertiary limestone).* RF4a and RF4b represent moderate- to low-amplitude horizontal reflection pattern (Fig. 5.5a, b). Towards the northern end of the radargram, poor amplitude reflections are observed. The poor amplitude response is due to clay rich content in Tertiary rocks. *(iii) RF1a and RF1b (Quaternary deposits).* Mesozoic (RF3a) and Tertiary rocks (RF4a and RF4b) are in disconformable contact with the overlying thick highly deformed Early Quaternary alluvial deposits (RF1b). It is represented by long, continuous moderate-amplitude reflections towards the southern side of the radargram, which turn into continuous, poor amplitude reflections towards the northern end of the radargram (Fig.

5.5a, b). Late Quaternary surficial, loose soil deposits are represented by continuous low-amplitude reflections of RF1a. The thin cover of RF1a overlying RF1b pinch out towards the southern end of GPR section. Note that no colluvial wedge deposits (RF2) is documented from this site.

(iv) Tectonic interpretation. At ~15 m horizontal distance, the subsurface presence of KMF is marked by – (i) sudden truncation of reflectors, (ii) abrupt change in dip of the continuous, sub-horizontal reflectors and, (iii) thinning-thickening of the reflectors. Also, in detailed view, warping of few reflectors can be observed across the KMF. The KMF as seen in the radargram is inferred as a north-dipping normal fault to the NW of Ghuneri dome (Fig. 5.5a, b). The KMF trace does not extend upwards into RF1b of Quaternary deposits. Any radar signature of the KMF in the overlying Quaternary deposits is not observed. The magnitude-based plot in Fig. 5.5c clearly demonstrate the position of the KMF in the radargram, which complements the radar observations from the linescan plot in Fig. 5.5a. The Mesozoic rocks are marked in the magnitude plot by high-energy contours, which continue to exist laterally up to the KMF (Fig. 5.5c). They transform into low-energy contours of Tertiary rocks towards the footwall of KMF.

Multiple small-scale slip planes with normal movement are observed in RF3a of Mesozoic rocks and RF4a and RF4b of Tertiary rocks. Few slip planes extend upwards into highly deformed alluvium of RF1b indicating their neotectonically active nature (Fig. 5.5a, b). Sudden truncation and displacement of reflectors mark the existence of slip planes. As the energy contours terminate along the slip planes, the magnitude-based plot also affirms their presence (Fig. 5.5c). Thus, the Hilbert transform using magnitude attribute illustrates the almost vertical low-frequency anomalies throughout the GPR section depth (Lunina et al., 2016).

Site 3

This site is located at the western flank of the Ghuneri dome (Fig. 3.1). The Tertiary rocks are exposed as almost vertical beds of nummulitic limestone, while the Mesozoic rocks are exposed as hard, well-compacted, baked sandstone beds. The GPR profile was acquired using 80 MHz antenna from south to north for a horizontal distance of 30 m (Fig. 5.6a). The southern side of the radargram shows the large, clear amplitude reflection pattern from the Mesozoic rocks while the northern side marks the poor, low amplitude reflection pattern on account of energy loss from the Tertiary rocks (Fig.

5.6a, b, c). Both the rock types are covered by ~2 m thick Quaternary alluvial cover (Fig. 5.6a). Fault plane is identified in the processed radargram at a horizontal distance of ~17 m. Across the fault plane, there is an abrupt truncation of the long, continuous reflectors and also an abrupt change in dip of reflectors can be seen. It can be inferred from the radargram that the KMF at the western flank of Ghuneri dome acts as a vertical fault in the subsurface.

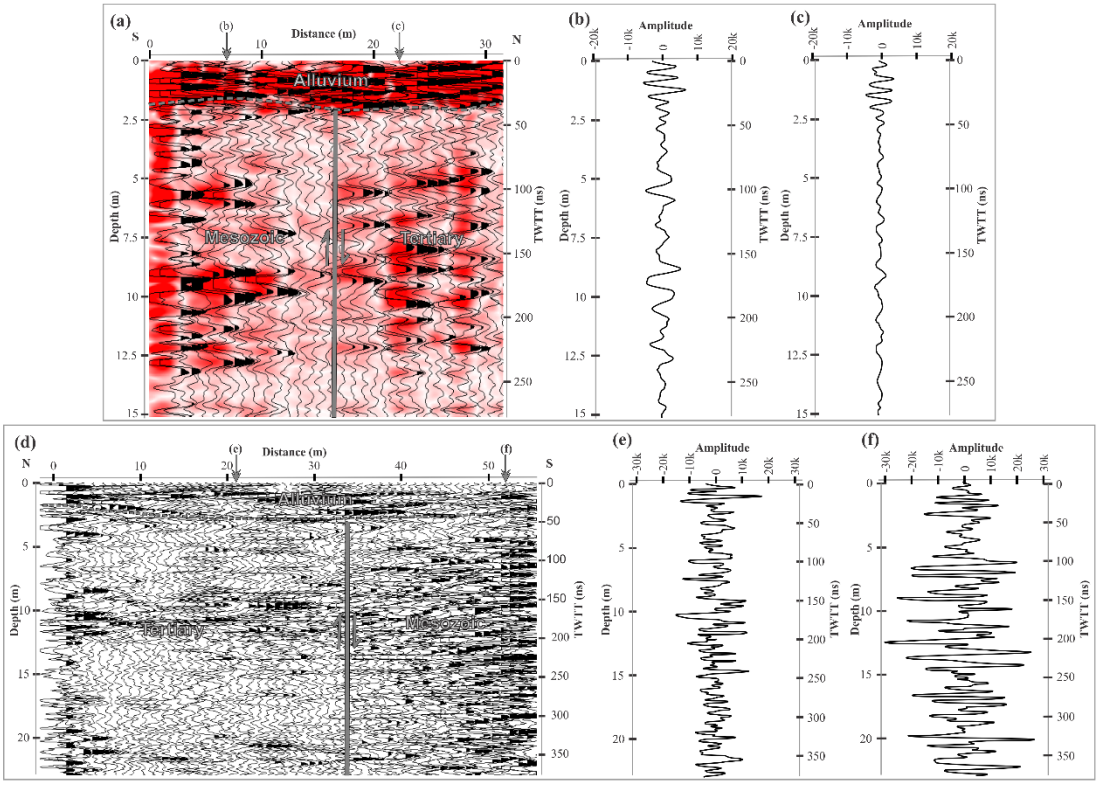

Fig. 5.6. Processed GPR radargrams (a) trace envelope based on magnitude draped over wiggle traces from 80 MHz antenna recorded across the KMF line at western flank of Ghuneri dome (site 3), location of site is shown in Fig. 3.1. The KMF can be easily appreciated at ~17 m distance as a vertical fault. Down arrows at top of profile (marked as (b) and (c)) indicate the position of single scan in oscilloscope format. (b) and (c) shows individual reflected waveform from Mesozoic rocks and Tertiary rocks respectively. (d) Wiggle traces acquired from 80 MHz antenna recorded across the KMF line at the eastern flank of Ghuneri dome (site 4), location of site is shown in Fig. 3.1. The high amplitude reflectors at the top of profile represent ~2 m thick Quaternary alluvial cover. The KMF is inferred to be vertical at ~34 m distance considering truncation of reflectors. (e) and (f) shows respective single scans for Mesozoic and Tertiary rocks.

Site 4

This site is located at the eastern flank of the Ghuneri dome (Fig. 3.1). Here, the strike of the KMF is found to be NW-SE. Mesozoic rocks are exposed as almost vertical sandstone beds while the Tertiary rocks are by conglomerate bed of Paleocene age. The average trend of beds is N130º. The GPR profile was acquired for a distance of 55 m in N240º orientation, perpendicular to the strike of the KMF using 80 MHz bistatic antennae in point mode (Fig. 5.6d). The southern side of the radargram shows radar facies corresponding to the Mesozoic rocks while the northern side of the radargram shows the radar facies corresponding to the Tertiary rocks. The KMF is found to be at a horizontal distance of 34 m in the radargram and is identified by the termination of the continuous reflections and attenuation of amplitude signals (Fig. 5.6d, e, f).

Site 5

Site 5 is located near Sahera village (Fig. 3.1) where the strike of the KMF switches to NNW-SSE. The change in the strike of KMF may be due to the oblique-slip motion along a NW-SE striking GUF which end up in the deformation zone of the KMF near Sahera. The highly deformed compacted Mesozoic sandstones are exposed in patches at the southern side while the Tertiary limestones rich in loose reddish clay are exposed to the north. 40 m long north-oriented cross-section with a time window of 100 ns, run approximately perpendicular to the strike of the KMF and parallel to a nearby small river channel (Fig. 5.7).

The radargram exhibit variation in reflection characteristics and are divided into radar facies – RF1 to RF4. The radargram consists of Quaternary deposits depicted by RF1a, RF1b and RF2, Mesozoic sandstones represented by RF3a and RF3b, Tertiary limestones portrayed by RF4a and RF4b (Fig. 5.7b). The radar characteristics of each of the radar facies are detailed below:

(i) RF1a, RF1b and RF2 (Quaternary deposits). RF1a, RF1b and RF2 are quite different from those observed in radargrams recorded across the KMF near Lakhpat. This variance in the radar response characteristics may be attributed to different processing parameters utilized during survey operation and also, the acquisition of radargrams were made during different field seasons. The uppermost dotted line at less than 1 m depth, represents the conformable contact between the youngest surficial loose soil sediments (RF1a) and underlying Early Quaternary deposits (RF1b) (Fig. 5.7a, b).

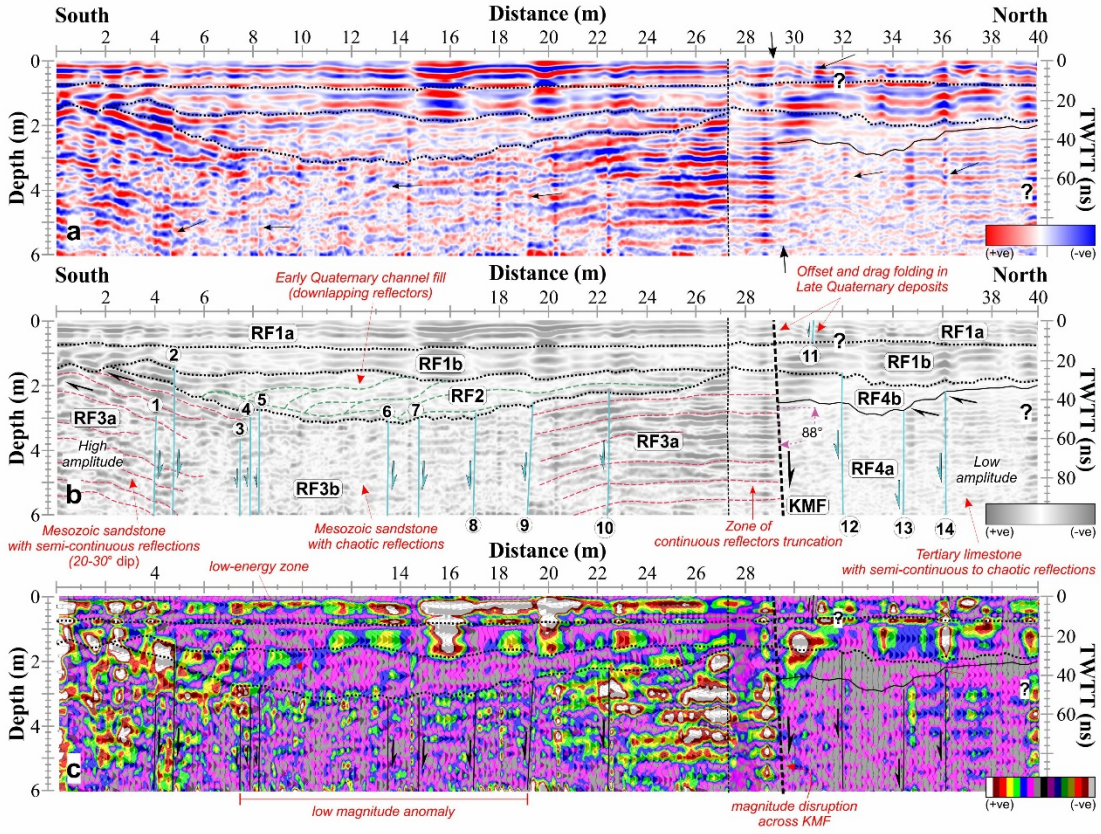

Fig. 5.7. 40 m long, north oriented GPR data recorded across the KMF, near Sahera village at site 5. See geological map of the study area in Fig. 3.1 for the location of GPR survey sites. Transect is taken over flat soil surface. Axis on left side shows penetration depth in meters and on right side two way travel time (TWTT) in ns is denoted. The upper axis shows section length in meters. Based on average subsurface radar wave velocity of 0.12 m ns^{-1}, radar arrivals have been translated to time-depth. Note that the direct air and ground waves have been muted in each of the plot formats. (a) Interpreted linescan plot. GPR amplitudes are represented by red (positive) and blue (negative) reflectors. Large arrows indicate the projected location of the KMF. Smaller arrows mark the interpreted position of secondary slip planes. Black dashed lines indicate conformable and non-conformable contacts between individual lithounits. (b) Interpreted sketch. From top to bottom, based on the reflectors response pattern, the cross-section is divided into radar facies RF1a – uppermost Late Quaternary valley-fill deposits, RF1b – Late Quaternary deposits, RF2 - Early Quaternary colluvium wedge-outs, RF3a - Mesozoic sandstone, RF3b – Mesozoic sandstone with chaotic reflections, RF4a and RF4b - Tertiary limestone deposits. Note the presence of Early Quaternary wedge-shaped deposits with onalpping and pinch over reflectors that terminate against the disconformable sediment (RF2)-bedrock (RF3a and RF4a) interface. (c) Trace envelope based on magnitude draped over wiggle traces. The color scale reflects the energy continuum, with white contours representing the highest-energy regions, while the lowest-energy regions are represented by grey contours. The lateral energy changes of EM waves clearly marks the presence of fault planes. Black lines indicate fault planes and half-arrows denote movement direction of the upthrown block in Figs. (b) and (c).

The hangingwall of the KMF is towards north and footwall is towards south. Note the presence of Early Quaternary channel-fill deposits (RF2) with tapering geometry and downlapping reflectors located in the footwall of the KMF. The steep northward dipping KMF with normal slip is interpreted to be located at ~29 m horizontal distance, which also extends upward into Quaternary deposits. The position of the KMF is inferred based on displacement, warping and truncation of continuous reflectors. Magnitude-based attribute in Fig. (c) supplements the presence of KMF as the high-energy contours of Mesozoic sandstone (RF3a) terminate against the KMF, which continue as low-energy contours of Tertiary limestone (RF4a and RF4b) in the hangingwall of KMF. The entire section is riddled with antithetic and synthetic slip planes with normal/reverse dip-slip motion.

RF1a, RF1b and RF2 occupy the upper 2–3 m depth and are perceived to be the responses from loose Quaternary sediments cover overlying the disconformable sediment-rock contact. Because the beds above and below the disconformity do not show much variation in inclination/dip, the contact cannot be considered a bounding surface. RF2 is located towards the footwall side of the KMF and is defined by concave shaped geometry with a horizontal length of ~25 m, resting over the RF3a and RF3b (deformed Mesozoic sandstones) (Fig. 5.7a, b). Sub-horizontal to gently dipping reflection pattern of RF2 emerges from Early Quaternary colluvial deposits, which along the slip planes are tapered on both sides. The low-amplitude zone of RF2 can be easily demarcated in magnitude-based attribute plot (Fig. 5.7c). Below the disconformity, RF3b also show poor magnitude response due to highly deformed zone. Towards north, the colluvial wedge appears to be truncated by the KMF. Note that no subisidiary fault offsets the colluvial wedge except slip plane 2 with normal slip (Fig. 5.7a, b). *(ii) RF3a and RF3b (Mesozoic sandstone).* On the southern side of the radargram, RF3a is observed to exhibit oppositely dipping converging reflectors pattern (20–30° dip) forming a form of fold, which is clearly expressed by the localized synclinal area (Liberty et al., 2003) (Fig. 5.7a, b). The semi-continuous reflections of RF3a representing the Mesozoic sandstone garde into chaotic reflections of RF3b representing the clastic, fine to coarse-grained sandstone. RF3b exhibit high attenuation caused by high electric conductivities, e.g. due to high clay content in Mesozoic rocks (Grützner et al., 2012) (Fig. 5.7c). *(iii) RF4a and RF4b (Tertiary limestone).* RF4a and RF4b demonstrate gently dipping to almost horizontal reflection pattern (Fig. 5.7). Towards the northern side of the radargram, in the hangingwall side of the KMF, the contact zone (30–50 ns depth) of Tertiary limestone deposits (RF4a and RF4b) and

overlying Quaternary alluvium deposits (RF1a) exhibits the bright amplitude, semi-continuous reflectors of RF4b (Fig. 5.7a, b). RF4a is represented by poor reflectivity and broken reflectors due to the contortion of GPR signals from the lower parts of the radargram. Clay rich, highly compacted beds of Tertiary limestone deposits are reflected in the form RF4a (Grützner et al., 2012). RF4b is showing flat, semi-continuous reflectors, which are tapering towards the northern side of the radargram.

(iv) Tectonic interpretation. 88° northward dipping KMF with normal slip-sense is inferred at ~29 m horizontal distance by observing the abrupt phase change in amplitude of the reflectors of RF3a (Fig. 5.7a, b). The abrupt change in amplitude is marked as RF3a show strong wide and long amplitudes cycles whereas RF4a and RF4b show weak and small amplitude cycles (Fig. 5.7a, b). The reflections also die out at the fault plane. The magnitude envelope attribute substantiates the interpretation as it also marks the presence of KMF (Fig. 5.7c). At ~27 m horizontal distance, in proximity to the KMF, another vertical discontinuity is identified. Because of the prevalence of compressive stress regime and structural complexities in the deformation zone of the KMF, multiple slip planes with normal slip (1–14) were recognised. None of the slip planes penetrate upwards into Quaternary deposits represented by RF1a, RF1b and RF2, lying above the disconformity, except the slip plane 11, which shows normal slip in the Late Quaternary deposits at 31 horizontal distance (Fig. 5.7a, b). This indicates that the majority of slip planes remained inactive in the Quaternary times. The radar characteristics used to pick the discontinuities are – (i) displacement of semi-continuous to broken, contorted reflectors clearly observed in the phase-based attribute and, (ii) an amplitude variation across the slip planes. Their position is also supported by the attribute plot for magnitude. Laterally, an abrupt transition in the energy pattern happens across the slip planes (Fig. 5.7c).

Site 6

This site is located to the northern extremity of the Mundhan anticline (Fig. 3.1). Almost vertically dipping, E-W trending, dark reddish, sheared, highly baked Mesozoic Jhuran sandstone beds are exposed which marks the approximate position of the KMF line. To the south of the exposure, undeformed sandstone beds are exposed. To the east of this location, loose, partially compacted conglomerate of Paleocene age are exposed on the Rann surface. The trend of the KMF here at the north of the Mundhan anticline is E-W. The GPR profile was acquired to the north of the scarp line, perpendicular to

the strike of the fault by 200 MHz antenna for a survey line of 37 m length with a time window of 125 ns. The true radar reflections in the raw GPR gather were severely contaminated and masked by the strong horizontal bands of ringing noise throughout the radargram. The radargram was processed according to the processing sequence proposed by Kim et al. (2007) to attenuate the reflections resulting from the ringing noise. Faulting was detected by observing the amplitude variations in the profile (Fig. 5.8d, e, f). The position of the fault in the processed radargram is marked by an abrupt change in the amplitude at 15 m horizontal distance. The sense of movement of the fault is interpreted to be almost vertical from the processed GPR profile.

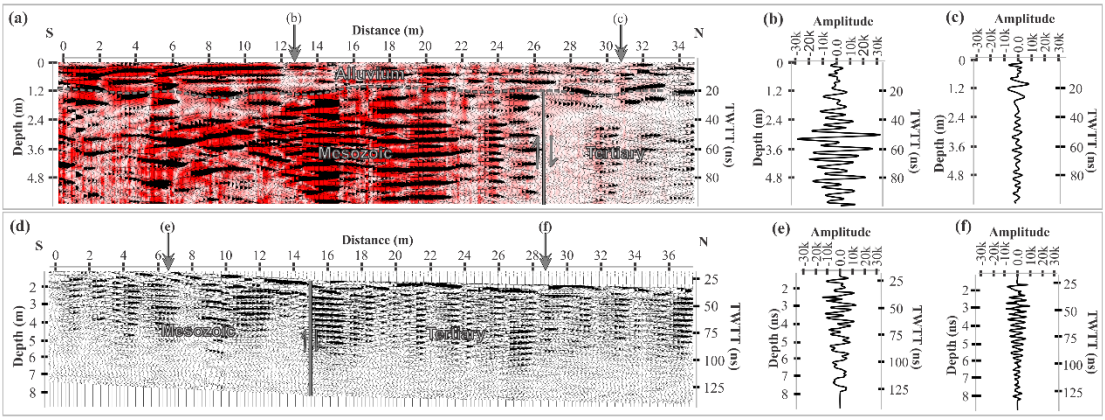

Fig. 5.8. Processed GPR radargrams (a) trace envelope based on magnitude draped over wiggle traces from 200 MHz antenna recorded across the KMF line at Sahera (site 5), location of site is shown in Fig. 3.1. The high amplitude reflectors at the top of profile represent 1.5 to 2 m thick Quaternary alluvial cover. The fault can be easily appreciated due to strong attenuation contrast & clear lateral discontinuity of the reflectors at ~26 m distance and inferred to vertical in geometry. Down arrows at the top of profile (marked as (b) and (c)) indicate the position of single scan in oscilloscope format. (b) and (c) shows the individual reflected waveform from Mesozoic rocks and Tertiary rocks respectively. (d) Wiggle traces acquired from 200 MHz antenna recorded across the KMF line at western flank of Mundhan anticline (site 6), location of site is shown in Fig. 3.1. The KMF is inferred to be a vertical fault at this site. (e) and (f) shows the respective single scans for Mesozoic and Tertiary rocks.

Site 7

The GPR surveys at sites 7, 8 and 9 were conducted few tens of meters north of Jumara dome, on the flat Great Rann surface. The KMF is certainly not located at the base of Jumara dome scarp. Because of long-term denudational processes, the fault scarp has experienced continuous retreat and therefore, the actual trace of the KMF is located further north of the base of scarp, which is buried below Great Rann surface.

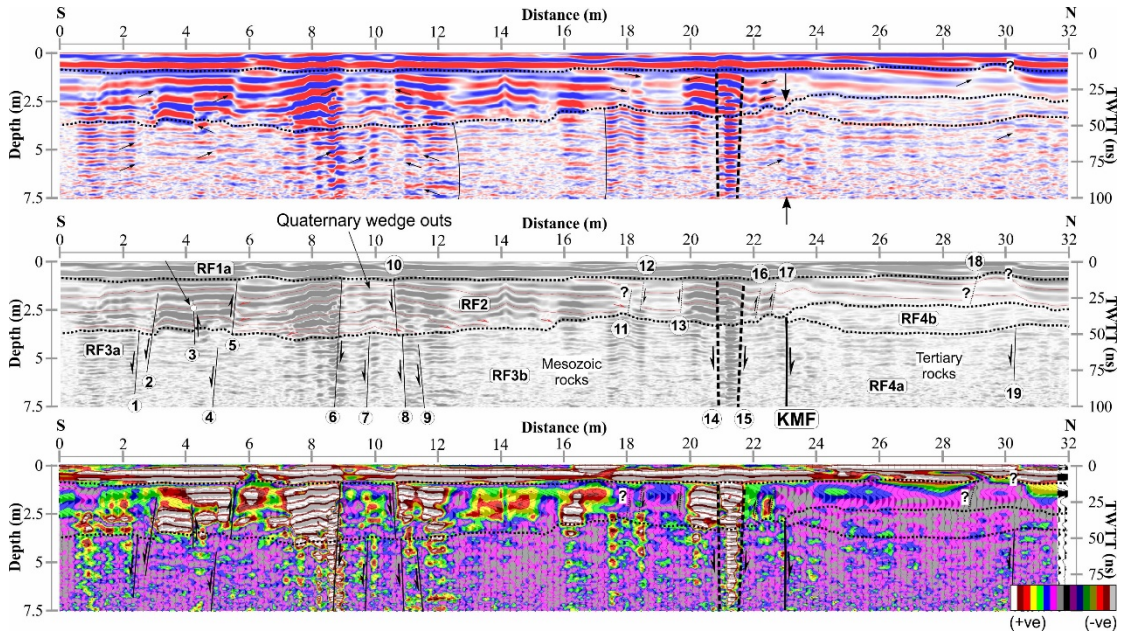

Fig. 5.9. 32 m long, north oriented GPR data recorded across the KMF, north of Jumara dome at site 7. See geological map of the study area in Fig. 3.1 for the location of GPR survey sites. Axis on left side shows penetration depth in meters and on right side two way travel time (TWTT) in ns is denoted. The upper axis shows section length in meters. Based on average subsurface radar wave velocity of 0.12 m ns^{-1}, radar arrivals have been translated to time-depth. Note that the direct air and ground waves have been muted in each of the plot formats. (a) Interpreted linescan plot. GPR amplitudes are represented by red (positive) and blue (negative) reflectors. Large arrows indicate the projected location of the KMF. Smaller arrows mark the interpreted position of secondary slip planes. Black dashed lines indicate conformable and non-conformable contacts between individual lithounits. (b) Interpreted sketch with lithology represented by colored lines. From top to bottom, based on the reflectors response pattern, the cross-section is divided into radar facies RF1a – uppermost Late Quaternary valley-fill deposits, RF2 - Early Quaternary colluvium wedge-outs, RF3a - Mesozoic sandstone, RF3b – Mesozoic sandstone with chaotic reflections, RF4a and RF4b - Tertiary limestone deposits. Note the presence of Early Quaternary wedge-shaped deposits with onalpping and pinch over reflectors that terminate against the disconformable sediment (RF2)-bedrock (RF3a and RF4a) interface. (c) Trace envelope based on magnitude draped over wiggle traces. The color scale reflects the energy continuum, with white contours representing the highest-energy regions, while the lowest-energy regions are represented by grey contours. The lateral energy changes of EM waves clearly marks the presence of fault planes. Black lines indicate fault planes and half-arrows denote movement direction of the upthrown block in Figs. (b) and (c).

The following radar facies were interpreted from the processed radargram – *(i) RF1a and RF2 (Quaternary deposits).* High-amplitude, thick, continuous reflectors of

RF2 represent thickest colluvial wedge deposits with maximum thickness of ~2 meters is observed at site 7 (Fig. 5.9a, b). The colluvial deposits wedge-out towards northern side of radargram. The reflectors of RF2 appears to be diverging from the low-amplitude anomaly located at ~10 m horizontal distance. It is to be noted that towards the southern side of radargram, colluvial wedge is marked by high-amplitude reflections in the footwall, while it is showing low-amplitude reflections in the hangingwall (Fig. 5.9a, b). This observation is also noted in the magnitude plot (Fig. 5.9c). RF1a is characterized by high-amplitude, long, continuous reflectors of Late Quaternary deposits concealing the colluvial wedge deposits. Note that no slip plane is affecting the Quaternary deposits of RF1a. The moderate- to low-amplitude reflections of RF1a are missing in the radargram recorded at site 7. *(ii) RF3a and RF3b (Mesozoic sandstone).* On the southern side of the radargram, at 0–8 m horizontal distance, low-amplitude, sub-horizontal, semi-continuous reflectors of RF3a are observed representing the Mesozoic sandstone (Fig. 5.9a, b). They grade into chaotic reflections of RF3b representing the clastic, fine to coarse-grained sandstone at 12–16 m horizontal distance. *(iii) RF4a and RF4b (Tertiary limestone).* In the hangingwall of KMF, the contact zone (30–50 ns depth) between Tertiary limestone deposits (RF4a) and overlying colluvial wedge deposits (RF2) exhibits the bright amplitude, flat, semi-continuous reflectors of RF4b (Fig. 5.9a, b). RF4b is tapering at the KMF. RF4a is represented by poor reflectivity and chaotic reflectors of clay rich Tertiary limestone deposits due to the contortion of GPR signals from the lower parts of the radargram. In the magnitude plot, Mesozoic sandstone (RF3a and RF3b) and Tertiary limestone (RF4a and RF4b) are marked by low-energy regions which are in clear contrast to high-energy contours of Quaternary deposits (RF1a and RF2) (Fig. 5.9c).

(iv) Tectonic interpretation. The inferred slip-sense of the high-angle northward dipping KMF at site 7, located at ~23 m horizontal distance in the radargram, is normal dip-slip as the footwall towards the southern side has moved up with respect to the hangingwall. The overlying Quaternary deposits of RF2 do not show any significant radar signatures that may mark the position of the KMF.

The radargram shows that the deformation zone is affected by arrays of subsidiary antithetic and synthetic faults. Between 1–6 m horizontal distance, the sense of shear of faults and sense of rotation of the individual fault blocks is not the same. Slip planes 1, 2 and 4 indicate normal slip, while reverse motion is seen in slip planes 3 and 5 (Fig. 5.9a, b). Since the dip direction of faults and slip-sense is not uniform, the

fault blocks cannot be termed as “dominos” (Stewart and Argent, 2000). Slip planes 2, 3 and 5 not only affects RF3a of Mesozoic sandstone, but they have been found to offset colluvium deposits of RF2, implying their neotectonically active nature (Fig. 5.9a, b). Slip plane 3 shows displacement and offset of reflectors, while other slip planes (e.g., slip plane 5) show twisting/bending of reflectors. The low-amplitude zone is also distinguishable in the magnitude plot as having low-energy contours (Fig. 5.9c).

Two distinct radar anomalies have been observed in the footwall side of the radargram – (i) low-amplitude anomaly at ~10 m horizontal distance and (ii) high-amplitude anomaly at ~21 m horizontal distance (Fig. 5.9a, b). At ~10 m horizontal distance, 2 m wide low-amplitude zone is located, which is fringed by conjugate reverse faults. Within this low-amplitude zone, several other slip planes with normal/reverse dip-slip are observed (Pousse-Beltran et al., 2018). The high-amplitude reflectors of RF2 at ~8 and 12 m horizontal distance abruptly transform laterally into low-amplitude anomaly indicate intense tectonic deformation of lithology. Note that in the magnitude plot, high-energy contours (marked by white color) on both sides of low-amplitude zone are truncated by slip planes (Fig. 5.9c). The low-amplitude anomaly persisted throughout the depth of the radargram disturbing the Mesozoic rocks and overlying Quaternary colluvial deposits. The low-amplitude anomaly is well-marked by low-magnitude contours in the magnitude plot as well (Fig. 5.9c).

In contrast to that, ~0.5 m wide high-amplitude anomaly at 21 m horizontal distance can be observed in the vicinity of the KMF. This high-amplitude anomaly also is fringed by two slip planes with normal slip, which are converging at depth. RF2 shows displacement of reflectors across the slip plane 14 located towards the southern side of high-amplitude anomaly. Whereas slip plane 15 shows only bending, twisting of reflectors of RF2 but do not show any displacement. Also, Mesozoic rocks of RF3a show abrupt amplitude change but do not show any displacement of reflectors across the high-amplitude zone. RF3 which is marked by white contours in the high-amplitude zone in the magnitude plot clearly are truncated along the slip planes at the fringe (Fig. 5.9c).

At ~6 m horizontal distance, sagging of reflectors of RF2 can be observed. However, the peculiarity of downward bending cannot be observed below in the reflectors of Mesozoic sandstones (RF3a). Towards the southern side, this localized sagging phenomena is obstructed due to the presence of slip plane 5 with reverse slip. Whereas towards the northern side, the downward dipping reflectors transform into

horizontal high-amplitude reflectors. Between 18–20 m window, two northward dipping slip planes with normal slip are noted in RF2, which encloses the low-amplitude displaced reflectors of RF2. Towards the hangingwall side of the KMF, the deformation structures are noted less in number as compared to the footwall. Note the off-fault folding noted in RF2 at ~30 m horizontal distance, which is accompanied by minor slip plane. The magnitude attribute draped over wiggle traces confirms the occurrence of multiple slip-planes (Fig. 5.9c). The phase-based attribute clearly enhances displacement, bending and twisting of reflectors across the slip planes. The unexpected shifts in the wavy reflection pattern in the wiggle plot specifically show the presence of deformed beds in the subsurface. The abrupt truncation of high magnitude contours often suggests the occurrence of subsurface discontinuity in the magnitude plot. Across the discontinuity, the high energy regions do not persist.

Site 8

The GPR section at site 8 was shot tens of meters north from the eastern flank of Jumara scarp. Southward dipping beds were noted at site 8, however, no such dip in beds were imaged in the radargram.

The radar facies observed are described below. *(i) RF1b (Quaternary deposits).* The uppermost dotted line at ~2-3 m depth, represents the disconformable contact between the Late Quaternary deposits (RF1b) and underlying Mesozoic (RF3a) and Tertiary rocks (RF4a) (Fig. 5.10a, b). RF1b is represented by high-amplitude, continuous reflections. The high-amplitude zone of RF1b can be easily demarcated in magnitude-based attribute plot (Fig. 5.10c). Note that the radar facies RF1a and RF2 are not present in the radargram. *(ii) RF3a (Mesozoic sandstone).* On the southern side of the radargram, RF3a is observed to exhibit high- to moderate-amplitude, wavy to sub-horizontal reflections (Fig. 5.10a, b). Low-amplitude, chaotic reflections of RF3b are not present in the radargram. *(iii) RF4a and RF4b (Tertiary limestone).* RF4a is in disconformable contact with the overlying Quaternary deposits (RF1b). RF4a exhibits low-amplitude, semi-continuous reflections with horizontal to gentle dip. RF4b demonstrate chaotic reflection pattern (Fig. 5.10a, b).

(iv) Tectonic interpretation. Steep northward dipping KMF with normal slip-sense is inferred at ~14 m horizontal distance. The sudden change in the amplitude of the reflectors of RF3a is noted (Fig. 5.10a, b). RF3a show strong amplitudes cycles whereas RF4a and RF4b show weak and small amplitude cycles (Fig. 5.10a, b).

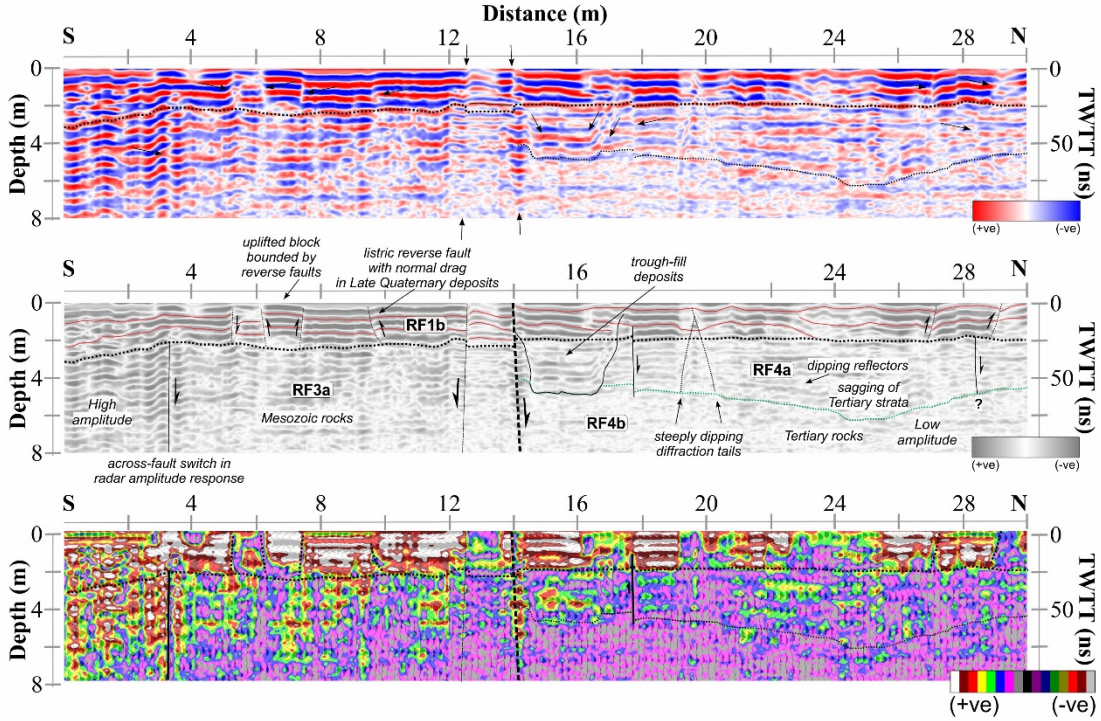

Fig. 5.10. 30 m long, north oriented GPR data recorded across the KMF, north of Jumara dome at site 8. See geological map of the study area in Fig. 3.1 for the location of GPR survey sites. At 20 m distance, the arrows (noise?) indicate steeply dipping diffraction tails affected by dispersion of EM waves. Axis on left side shows penetration depth in meters and on right side two way travel time (TWTT) in ns is denoted. The upper axis shows section length in meters. Based on average subsurface radar wave velocity of 0.12 m ns^{-1}, radar arrivals have been translated to time-depth. Note that the direct air and ground waves have been muted in each of the plot formats. (a) Interpreted linescan plot. GPR amplitudes are represented by red (positive) and blue (negative) reflectors. Large arrows indicate the projected location of the KMF. Smaller arrows mark the interpreted position of secondary slip planes. Black dashed lines indicate conformable and non-conformable contacts between individual lithounits. (b) Interpreted sketch with lithology represented by colored lines. From top to bottom, based on the reflectors response pattern, the cross-section is divided into radar facies RF1a – uppermost Late Quaternary valley-fill deposits, RF2 - Early Quaternary colluvium wedge-outs, RF3a - Mesozoic sandstone, RF4a and RF4b - Tertiary limestone deposits. Note the presence of Early Quaternary wedge-shaped deposits with onalpping and pinch over reflectors that terminate against the disconformable sediment (RF2)-bedrock (RF3a and RF4a) interface. (c) Trace envelope based on magnitude draped over wiggle traces. The color scale reflects the energy continuum, with white contours representing the highest-energy regions, while the lowest-energy regions are represented by grey contours. The lateral energy changes of EM waves clearly marks the presence of fault planes. Black lines indicate fault planes and half-arrows denote movement direction of the upthrown block in Figs. (b) and (c).

The reflections of RF3a also die out at the KMF. The magnitude-based attribute also supports the interpretation as high-energy contours of Mesozoic sandstone terminates along the KMF (Fig. 5.10c). Across the KMF, no significant displacement of continuous reflectors is observed. However, bending or twisting of reflectors clearly signifies the presence of KMF. Multiple discontinuities with normal slip are documented from Mesozoic rocks (RF3a) and Tertiary rocks (RF4a and RF4b). The normal fault interpreted at 3 m distance, which do not penetrate upwards into Quaternary deposits, show (i) displacement of reflectors and, (ii) abrupt change in radar amplitude response. Contrary to this, no amplitude change is observed along the southward dipping steep normal fault observed at ~13 m distance. The Mesozoic rocks do not show any signature of faulting, but overlying Quaternary deposits show warping of reflectors, which suggest smalls-scale fault related folding. Another steep normal fault is observed in RF4a. its presence is clearly marked by displaced reflectors and it also displaces the disconformable contact. The processed section revealed significant evidences for synthetic and antithetic faults with reverse/normal slip mainly localized in the upper Quaternary deposits (RF1b). The reflectors are displaced and distinct change in the dip can be observed. High energy contours in pockets in Quaternary deposits delimited by slip planes with normal/reverse slip (Fig. 5.10c).

Reflectors are disrupted and displaced alongside the KMF and subsidiary slip planes. Continuous sub-horizontal reflectors are greatly displaced within the upper part of the hangingwall in the vicinity of the KMF, forming a concave pattern that is perceived as deformed fault-related Late Quaternary channel-fill deposits. Offset of reflectors along the boundary of the trough-shaped pattern is observable. High-resolution GPR data shows concave-shaped internal reflections within the trough-fill structure in a close-view. The concave filling is related to the sedimentation induced due to tectonic movement along the KMF.

Small-scale north/south dipping reverse listric faults restricted to the upper Quaternary deposits are the characteristics of this radargram. The GPR data from no other site show the presence of listric faults. At 10 m distance, reverse listric fault with normal drag is observed as the reflectors in the hangingwall are convex-up as compared to the flat reflectors located in the footwall (Grasemann, 2005). At 5 m distance, uplifted block bounded by smalls-scale reverse faults is observed in Quaternary deposits.

Site 9

Site 9 is located tens of meters north of the Jumara scarp. Southward dipping beds were noted at site 9, however, no such dip in beds was imaged in the radargram. The observed radar facies are as follows – *(i) Moderate-amplitude RF1a representing the topmost Quaternary sediments cover*. RF1a is characterized by long, continuous reflectors (Fig. 5.11a, b). Their continuity is also expressed by relatively elliptical contours observed in the magnitude-based attribute plot (Fig. 5.11c). RF1a portrays the uppermost Holocene Rann sediments. The moderate- to low-amplitude reflections of RF1b representing Late Quaternary deposits are missing in the GPR profile at site 9. *(ii) Moderate- to low-amplitude semi-continuous RF2 indicating potential colluvial wedge.* The colluvial wedge deposits defined by RF2 are thickest (~2 m) towards the footwall block of the KMF, which, when approaching the hangingwall block, becomes pinch-off. The wedge in this case is more undulatory and the exact explanation why its thickness is greater above Mesozoic rocks should be known, whereas thinning is observed over Tertiary rocks. *(iii) High- to moderate-amplitude semi-continuous to broken RF3a and RF3b representing Mesozoic sandstone.* On the southern margin, RF3b is observed to exhibit low-amplitude, chaotic reflections (Fig. 5.11a, b). They laterally transform into semi-continuous high-amplitude reflections of RF3a. RF3a and RF3b radar facies represent Mesozoic sandstone deposits. *(iv) Low-amplitude chaotic RF4a representing Tertiary limestone.* RF4a is in disconformable contact with the overlying RF2 (colluvial deposits). RF4b radar facies is missing in the GPR section (Fig. 5.11a, b).

(v) Tectonic interpretation. At ~18 m distance, steep northward dipping KMF with normal slip-sense is inferred. No major displacement, bending or twisting of continuous reflectors is observed across the KMF. The amplitude response is also uniform across the KMF. There is, however, a major difference in the pattern of the reflectors, which marks the position of the KMF. Semi-continuous high-amplitude reflectors of RF3a convert laterally into low-amplitude chaotic reflections of RF4a. The magnitude-based attribute also supports the interpretation as high-energy contours of Mesozoic sandstone terminate along the KMF (Fig. 5.11c). Note that the KMF does not penetrate upwards into Quaternary deposits represented by RF1a and RF2.

Largely, the reflectors of RF1a are continuous and undeformed, but, at 10–12 m distance window, subsidiary slip planes with reverse motion are observed. The slip planes caused bending, twisting of reflectors of RF1a. The slip planes also displace the

conformable contact between RF1a and RF2. In RF2, intense zone of shearing is observed between 8–15 m distance. The normal/reverse slip planes that post-date the generation of colluvial wedge caused small, broken reflectors in this zone. Few slip planes are marked by the displacement on the order of one amplitude cycle. On the other hand, warping of reflectors is also clearly observed.

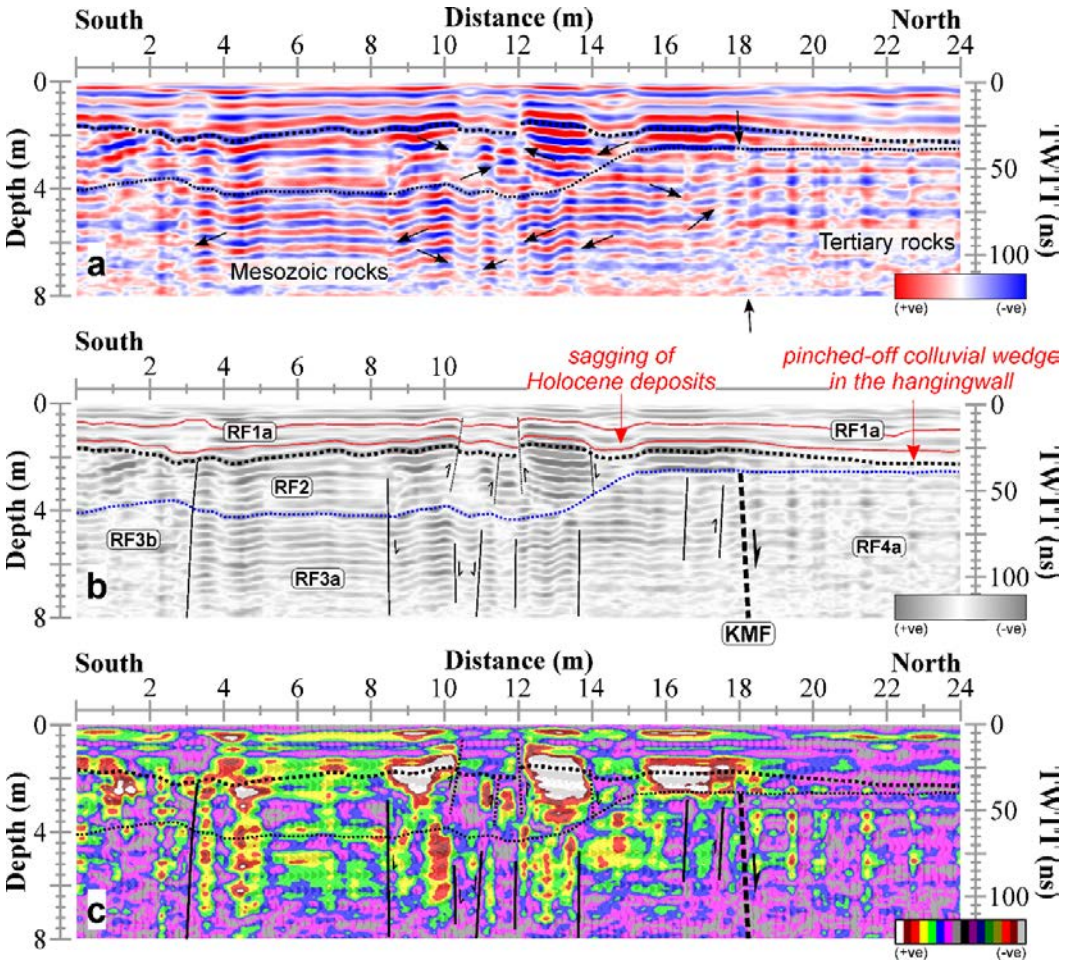

Fig. 5.11. 24 m long, north oriented GPR data recorded across the KMF, north of Jumara scarp at site 9. See geological map of the study area in Fig. 3.1 for the location of GPR survey sites. (a) Interpreted linescan plot. GPR amplitudes are represented by red (positive) and blue (negative) reflectors. Large arrows indicate the projected location of the KMF. Smaller arrows mark the interpreted position of secondary slip planes. Black dashed lines indicate conformable and non-conformable contacts between individual lithounits. (b) Interpreted sketch with lithology represented by colored lines. (c) Trace envelope based on magnitude draped over wiggle traces. The color scale reflects the energy continuum, with white contours representing the highest-energy regions, while the lowest-energy regions are represented by grey contours. The lateral energy changes of EM waves clearly marks the presence of fault planes. Black lines indicate fault planes and half-arrows denote movement direction of the upthrown block in Figs. (b) and (c).

The lateral continuity of chaotic reflections of RF3b is hindered at ~3 m distance by the slip plane with unknown slip-sense. The presence of the slip plane is marked only on the basis of the abrupt lateral shift in the reflections pattern. Across the slip plane, the chaotic reflections convert into semi-continuous reflections with high-amplitude. Note that no displacement is observed among the reflectors. This slip plane penetrates upwards and also disturbs Late Quaternary colluvial deposits represented by RF2. The almost horizontal continuous reflections of RF3a continue up to the normal slip plane present at ~8 m horizontal distance. Beyond this slip plane, semi-continuous reflections of RF3a transform into wavy, broken, reflections between 8–14 m distance. This zone of RF3a is affected by several slip planes with normal/reverse slip-sense indicating highly deformed Mesozoic sandstone. The presence of slip planes is also marked by small oval-shaped contours in the magnitude-based attribute plot (Fig. 5.11c). At ~14 m distance, the broken reflectors of RF3a again transform into semi-continuous reflections.

SHALLOW SUBSURFACE NATURE OF THE KMF

Extensive high-resolution shallow subsurface geophysical surveys were performed during field investigations to document the neotectonically active nature of the concealed KMF and related subsidiary slip planes and to demonstrate the radar characteristics of the fault deformation zone. The geophysical studies directly map the deformation features and colluvial wedges generated due to periodic tectonic movements along the KMF. Since the KMF is largely buried underneath alluvial cover in the western part of the KRB, there are only a few sites where geophysical surveys across the fault could be performed. Most of these sites exist a few tens of meters north of structural domes located on the upthrown block of the KMF. GPR data were recorded across the KMF where in the case of normal dip-slip motion, hangingwall consists of Tertiary limestone and footwall comprises Mesozoic sandstone. Most of the radargrams presented in this work have been shot with the 200 MHz antenna. The survey line run perpendicular to the main fault. The depth of penetration portrayed is 100–150 ns TWTT. Most of the sites exposes numerous secondary fault strands associated with the KMF. In the Jara and Jumara domes, tectono-geomorphic and structural studies carried out by Shaikh et al. (2019) suggest latest dip-slip movement occurred during in the western part of the KRB. Slip definitely occur along blind secondary fault strands of the KMF and fault offsets in younger Quaternary sediments inferred from GPR cross-

sections are the accurate measures of the recent seismicity in the study area. The buried KMF can be traced using GPR in terms of distance and projected to the uncovered outcrop. Thus, GPR data across buried KMF from several locations are compared to the outcrop exposures wherever they are available. The illustrations indicate that high-resolution GPR data not only offers the ability to trace and map buried active faults, but also to visualize the associated subsidiary, multiple slip planes; fault-scarp associated deformed sedimentary structures in the subsurface in the fault zone, such as coarse-grained clastic colluvial wedges, folded strata, truncated river channel. Thus, the existence of the buried active faults are usually linked with well-defined deformed sedimentary structures preserved in the fault zone (tapering colluvial wedges, channel-fill deposits in the uplifted block). High-resolution GPR is considered as an alternate tool in pre-trenching paleoseismological studies. New GPR findings are documented from the KMF damage zone that shed light on the slip geometry and fault orientation and associated structures up to a depth of 10 m. This contribution also covers approaches of GPR data interpretation and ways of fault imaging.

Detailed GPR investigations were carried out at selected sites after intensive field studies. The GPR data recorded were processed and interpreted in light of field observations. In each of the 200 MHz GPR profiles, the maximum depth of penetration achieved is <~8 m. In general, all profiles clearly demarcate the lithological contrast across the fault plane that has been helpful in highlighting the position of the KMF in the radargrams. The Mesozoic rocks comprising hard, well-compacted sandstones yielded high-amplitude radar reflection events while the relatively the Tertiary rocks exhibiting the different dielectric properties showed attenuation of radar waves. The sharp amplitude contrast along the length of the radargram is interpreted as the trace of the KMF.

The KMF is the lithotectonic contact between the Mesozoic rocks (RF3a and RF3b) exposed in the NHRFZ in the upthrown block and the Tertiary rocks (RF4a and RF4b) exposed in the form of thin strips in the northern downthrown side of the fault, mostly covered by thin cover of Quaternary sediments (RF1a, RF1b and RF2) of Great Rann basin. The surficial occurrence of the KMF is not continuous and is largely blanketed by thin cover of Quaternary sediments. RF1b and RF2 representing the Quaternary sediments are stratified and faulted internally, as indicated by small, subsidiary slip planes with normal/reverse dip-slip motion. Pinching out structures are interpreted as forming coarse-grained colluvial wedges. While at the edges of fault

blocks or the subsurface presence of large boulders, diffraction hyperbolae form, none of the radargrams in the present study attest to their existence (Grützner et al., 2012). Between Lakhpat anticline and Ghuneri dome, the KMF, at places is buried under thin cover of miliolite deposits. The present-day landscape shows youthful topography, knickpoints and incised drainages indicating the ongoing neotectonic activity along the KMF (Shaikh et al., 2019).

Since several of the buried secondary faults offset or disrupt Quaternary sediments, they can be categorized as neotectonically active. Since the seismicity is majorly recorded from the eastern part of the KRB, the subsurface evidences presented in this contribution, point that the western part of the KMF should not be neglected despite being showing low levels of seismicity. The structural evidences inferred from the GPR data indicate that this region of the KRB is also tectonically unstable.

Colluvial wedges have been imaged with the help of a range of geophysical techniques. Colluvial wedges have been imaged with seismic traveltime and waveform tomography techniques (Wasatch Fault, Utah: Buddensiek et al., 2008). Electrical resistivity tomography (ERT) technique can also be used to detect the colluvial wedges (McCalpin, 2009). Vanneste et al. (2006) identified three colluvial wedges in the hangingwall of the fault and deciphered at least three surface-rupturing paleo-earthquakes in southern Bulgaria. Christie et al. (2009), Carpentier (2012a), (2012b) images colluvial wedges using GPR.

McCalpin (2009) state that seismic reflection technique could not differentiate colluvial wedges 1 to 2 m thick. P-wave seismic refraction tomography performed by Sheley et al. (2003) and other authors identified the colluvial wedges as low-velocity zones. The largest wedge could not be identified in the tomograms, and there were many small low-velocity zones in the tomogram that did not correspond to any colluvial wedge. McCalpin (2009) state that massive, moist saline soils are opaque to GPR response. However, prehistoric colluvial wedges formed of dry gravels can be detected. In such scenario, GPR technique has been found effective in mapping the subsurface occurrence of colluvial wedge in the deformation zone of the KMF. This technique can be extensively used in other depositional environments.

The outlines of the scarp-derived colluvial wedge network and their internal structures in each of the GPR section are described. The concealed earthquake-related structures, e.g., colluvial wedges, off-fault folding, secondary slip planes should be imaged by geophysical techniques to evaluate the neotectonic activity along the fault

(Pavan Kumar et al., 2018). Sheley et al. (2003) interpret that in their 2D refraction tomograms, the lowest velocity regions beneath the fault scarps corresponded to the scarp-derived colluvial wedge. Same is observed in the present study. The colluvial wedges in the GPR data represent low amplitude zone and in the magnitude attribute also, low-energy zone is identified easily. The colluvial wedges, which are unique features that indicate co-seismic displacement (McCalpin, 2009), are distinguished in the present study by reflections of low-amplitude, typically seen in coarse-grained sediments. The wedges consist predominantly of blocky clasts of Bhuj sandstone and Tertiary limestone deposits. The material that gathers at the base of steep mountain slopes is colluvium (Christie et al., 2009). As a result of fault scarp weathering and retreat and redeposition of footwall detritus at the scarp toe over time, colluvial wedges form at the base of fault scarp (McCalpin, 1996; Christie et al., 2009). Colluvial wedges are derived from the uplifted block of Northern Hill Range (NHR) that has endured long-term erosion due to periodic tectonic movement along the KMF (Shaikh et al., 2019). The detection of wedge-shaped colluvial geometry in the landscape undergoing long-term rejuvenation demands significant effort. The tapered colluvial wedges are wrapped by the scarp-derived wash-off sediments, which are characterized by thick, long, continuous, parallel reflections suggesting well-stratified Late Quaternary deposits, reflecting a period of seismic quiescence. Note that none of the GPR radargrams presented in this work record multiple colluvial wedges. All the wedges documented are in contact with the KMF and overlie it and few of them are also affected and displaced by KMF. At site 5, the colluvial wedge is translocated to the footwall (towards the southern side). All the colluvial wedges thicken towards the main strand of KMF. The existence of colluvial wedges confirm the geophysical evidence for earthquake-related faulting. The on-fault scarp-derived colluvial wedges represent post-seismic delayed response of the tectonic deformation along the KMF. The formation of colluvial wedges in the all the cases in the vicinity of structural domes represent single faulting event. In site 5 radargram, folding of beds of Quaternary deposits representing colluvial wedges above the KMF can be observed. The thickness of colluvial wedges in fault exposures can be used to estimate the magnitude of earthquake. Amount of fault displacement can also be estimated using the thickness of colluvial wedges (McCalpin, 2009).

The wedge-shaped geometry in the case of site 5 reflects a depositional package related to a paleo-river erosional channel truncated by the displacement and uplift along

the KMF near Sahera. As the radargram is taken near north-flowing river channel, the Early Quaternary wedge-out material recorded in the GPR data at site 5 near Sahera village may represent paleo-channel fill deposits. The channel-cut geometry picked by the GPR section reflect the paleo-course of the present-day arid river channel nearby. Later on, the paleo-course may have been truncated by the neotectonic movement along the KMF, which altered the course of channel causing channel shift/migration. In such tectonically sensitive terrains, the flowing channel deposits its own sediments that are considered terrace deposits. Because of the upliftment in the tectonically active terrain, the river could not change its course. It simply cut its course and formed a new channel by shifting its course. Therefore, it is inferred that the GPR survey was recorded over the terrace surface of the nearby flowing channel.